[Short title + Author Name - P&H title] 17 (2024) 105599

Contents lists available at ScienceDirect

Arabian Journal of Chemistry

journal homepage: www.ksu.edu.sa

The effective adsorption of Ni(II) and nitrate from aquatic systems by superparamagnetic $MoS_2/\gamma\text{-}Fe_2O_3$ nanocomposites: Optimization through RSM-CCD design

Somayeh Ostovar *, Hamideh Saravani *, Maryam Akbari, Amanolah Salehpour, Mohammad Sabaghi, Esmaiel Rezazadeh

Department of Chemistry, University of Sistan and Baluchestan, Faculty of Sciences, PO Box 98135-674, Zahedan, Iran

ARTICLE INFO

Keywords:
Adsorption capability
Central composite design
Response surface methodology
Superparamagnetic nanocomposite

ABSTRACT

In this study, we examined the adsorption capacity (Qe) of superparamagnetic $MoS_2/\gamma\text{-}Fe_2O_3$ nanocomposite with varying percentages of loaded $\gamma\text{-}Fe_2O_3$ nanoparticles (10 %, 20 %, and 30 %) for rapid and effective removal of Ni^{+2} and NO_3^- ions from water using response surface methodology combined with the central composite design (RSM-CCD). In essence, the adsorption properties of MoS_2 3D ball-flower-like are increased by loaded $\gamma\text{-}Fe_2O_3$ nanoparticles by forming nanocomposite. Magnetic nanocomposites were checked under optimum conditions to remove Ni^{+2} and NO_3^- ions several times, which showed the material's ability for regeneration and reuse as adsorptions. In experimental design, in the first step, we attempt to present models for the adsorption capacity (Qe) and removal percent and detect the influence of the parameters of the process using response surface methodology (RSM) by historical data. In the next step, with regard to the detection of impressive variables using obtained results in the previous step, the central composite design (CCD), by consideration of independent variables for the experimental design was done. By interpreting ANOVA and diagnostic plots, the effect of individual and binary effect of variables was discussed. The optimal conditions for maximizing adsorption capacity (Qe) and removal percent were predicted, and the validation of the predicted conditions was experimentally evaluated, which confirmed an agreeable agreement. The optimization of predicted conditions for Ni^{+2} and NO_3^- species are reported in the concentration of (0.49 mol.L^{-1}) Ni^{+2} and (0.50 × 10^{-4} mol.L^{-1}) NO_3^- with weight percent of $\gamma\text{-}Fe_2O_3$ = 26.72 % and 27.55 %, respectively. Predicted adsorption capacity (Qe) and removal percent of species concentration for Ni^{+2} and NO_3^- ions of optimized nanocomposite concluded 0.98, 9.59 × 10^{-5} (mg/g), 100, and 96 (%), respectively, which was confirmed by experimental research studies. To optimize experimental conditions, the Ni^{+2} and NO_3^- concentrations were o.5 and 0.5 × 10^{-4} mol.L^{-1}, respectively. Furthermore, nanocomposites of $MoS_2/\gamma\text{-}Fe_2O_3$ with a loaded dose of 26.72 % and 27.55 % $\gamma\text{-}Fe_2O_3$ for Ni^{+2} and NO_3^- were synthesized, respectively. The experimental of the adsorption capacity (Qe) and removal percent of species concentration for Ni^{+2} and NO_3^- ions concluded 0.95, 9.23 × 10^{-5} (mg/g), 96, and 93 (%) using $MoS_2/\gamma\text{-}Fe_2O_3$, respectively.

1. Introduction

In view of rapid growth in industrialization, population, and urbanization, the disposal of untreated organic/ inorganic toxic effluents from aqueous media remains a great challenge for public health and environmental protection (Madima et al., 2020; Kiani et al., 2021; Alsubih et al., 2022; Anderson et al., 2022; Ostovar et al., 2023b). Wastewater discharge without proper treatment leads to increased environmental pollution that affects the quality of surface and groundwater resources (Runnan Zhang et al., 2016; Choudhary et al., 2020; Kesari et al., 2021). These distressing situations for human beings and ecosystems have led to creating of novelty strategies to increase water quality for the purification of the wastewater process and to preserve freshwater sources (Ighalo and Adeniyi, 2020; Hmoud Al-Adhaileh and Waselallah Alsaade, 2021). A promising strategy for the purification of wastewater and to preserve freshwater sources has developed various

* Corresponding authors.
E-mail addresses: somayeh.ostovar.s@gmail.com (S. Ostovar), saravani@chem.usb.ac.ir (H. Saravani).

https://doi.org/10.1016/j.arabjc.2024.105599
Received 2 July 2023; Accepted 1 January 2024
Available online 2 January 2024

water treatment technologies for both industrial applications and environmental remediation (Hao et al., 2020; Hoang et al., 2022; Amanollahi et al., 2023; Ostovar et al., 2023a).

Among various wastewater remediation techniques, (Bolisetty et al., 2019; Ostovar et al., 2023a; Rahman et al., 2023a) membrane filtration, (Buruga et al., 2019; Pronk et al., 2019; Torkashvand et al., 2022) flocculation, (Abujazar et al., 2022) adsorption, (Bahrami and Amiri, 2022) chemical precipitation, (Benalia et al., 2022) ion exchange, (Swanckaert et al., 2022) conventional coagulation, (Abujazar et al., 2022) electrodialysis, (Sedighi et al., 2023) electrolytic removal, (Setayesh et al., 2020) reduction (Goswami et al., 2022) and reverse osmosis (Sudesh Yadav et al., 2020) have been reported as efficient methods to eliminate pollutants from wastewater. However, various limitations for these technologies such as costly equipment, high operational cost, high maintenance cost, partial metal ions removal, high energy requirement, and lethal residual metal sludge are presented (Chakraborty et al., 2022; Hoang et al., 2022; Mahmoudian et al., 2023). Among these techniques, adsorption technique including activated carbon, (Mariana et al., 2021; Xiaohong Wang et al., 2022) zeolite, (Rad and Anbia, 2021) clays, (Benhammou et al., 2005; Lahnafi et al., 2022) and waste biomass (Maharana et al., 2021; Yingjun Wang et al., 2021) is suggested as conventional adsorbents to purify water due to its high efficiency (Singh and Pant, 2004; Rahman and Khan, 2016; Fei and Hu, 2022), simplicity (Sheth et al., 2021; Wang et al., 2021), and cost-effectiveness (Singh et al., 2020; Maharana et al., 2021) with minimal waste production (NB Singh et al., 2018; Saleh et al., 2022). A key challenge is to determine target contaminant selectivity with competitive adsorption among these adsorptions that have often poor selectivity. Therefore, producing complex components compromises adsorption performance to treat water (Wang et al., 2017a; Pincus et al., 2019; Yang et al., 2021). The main aim is to create strong interactions between target contaminants and adsorbents that will achieve adsorbents with high capacity and selectivity (Ma et al., 2016; Ali et al., 2021; Liu et al., 2023). Three basic categories of the chemical contaminants in water including organic, inorganic, and radioactive have been reported, subsequently, several classes of contaminants have been identified within each of these categories (Brusseau and Artiola, 2019; Jun et al., 2021). In turn, Heavy Metal Ions (HMIs) such as arsenic, lead, cadmium, nickel, chromium, zinc, copper, mercury, cobalt, etc. have been introduced as a class of inorganic pollutants as one of the most hazardous species (Vidu et al., 2020; Numan et al., 2021). Due to their toxic nature, heavy metal ions (HMIs) that are added in water resources from different industries like mining, metal plating industries, batteries, painting, tanneries, fertilizer, etc. are a critical threat to healthy ecosystems (Vijay Bahadur Yadav et al., 2019; Ghomi Avili, 2021). The excess amounts of nitrates in groundwaters as a consequence of the intensive use of fertilizers and other anthropogenic sources, such as sewage or industrial wastewater discharge can cause significant water quality problems (Abascal et al., 2022). Recently, to improve the obtained outcomes of the removal of heavy metallic species from water for environmental remediation, active nanoparticles such as nano- adsorbents (Tingting Zhang et al., 2021; Janani et al., 2022), nano-catalysts (Lande et al., 2020; Lu et al., 2022; Sheerazi and Ahmed, 2022), and biological techniques (Priyadarshanee and Das, 2021) are being implemented for water treatment, which have attracted more attention from researchers. Nanostructured materials with small dimensions have a high specific surface area, and surface area to volume' ratio, while due to these exceptional features, a great number of active sites by catalytic potential and high reactivity have advanced the removal efficiency of the nanostructured materials (Bethi et al., 2016; Choi and Lee, 2022; Ostovar et al., 2023a). Numerous adsorbents for HMIs removal from the contaminated water such as activated carbon (Gusain et al., 2020), biomaterials (Kothavale et al., 2022), clay/layered double hydroxides (Kumar et al., 2017; Kong et al., 2019), hydrogels (Ma et al., 2017), zeolites (Huang et al., 2018), silica gel (Niu et al., 2013), and nanocomposites have been reported (Alqadami et al., 2017; Zhao et al., 2019). Some disadvantages of nano adsorbent materials such as low specific active surface area and poor selectivity have been proved. Recently, researchers have been looking for promising nano- adsorbents to eliminate HMIs from water sources (Harja and Ciobanu, 2020; Thangadurai et al., 2020; Vishwakarma, 2021; Zangiabadi and Yazdapanah, 2021). For example, two-dimensional (2D) nanomaterials, such as graphenes (Gs), molybdenum disulfide (MoS_2), and carbon nanotubes (CNTs) applied as adsorbents (Ren et al., 2011; Shen and Chen, 2015; Yu et al., 2015). Among these nanomaterials, flower-like molybdenum disulfide (MoS_2) has been employed in various fields such as energy storage and transformation, environment protection, and biomedicine. Its unique physicochemical properties include various prominent chemical, electronic, catalytic, optical, mechanical, and sensing properties (Najmaei et al., 2014; Singh et al., 2016; Barua et al., 2017; Wang et al., 2017b; Li et al., 2020). On the other hand, due to the abundance of intrinsic sulfur atoms in layered MoS_2 nanosheets, they are reported as the efficient purification of water polluted by HMIs (Xu et al., 2020). The research studied in this field shows that heavy metals have been removed with high selectivity using sulfur-containing or sulfur functionalized adsorbents (Wang and Mi, 2017). The sulfur in adsorbents has a high affinity to heavy metal ions via Lewis soft–soft interactions that lead to superior adsorbents (Ma et al., 2016; Manos and Kanatzidis, 2016; Zhang et al., 2017b). Nanosheet samples possess better properties than those of bulk ones because sulfur atoms located on both sides of a sheet lead to good accessibility of adsorption sites, and thus show an absorption capacity higher than the capacity of the best adsorbents (Liu et al., 2015; Tanweer et al., 2022). Numerous studies have been reported on the adsorption of toxic heavy metal ions such as Hg(II) (Wang et al., 2018), Co(II) (Aghagoli et al., 2017), Cr(VI) (Wang et al., 2017a), Pb(II) (Chang Liu et al., 2017), and Ni(II) (Aghagoli and Shemirani, 2017) by 2D nanosheets and 3D ball-flower-like molybdenum disulfide (MoS_2). Another challenge after removal of HMIs is separating the material for secondary recycling that has been suggested using a magnetic transition metal to facilitate recovery. Identified properties ofFe_3O_4 nanoparticles such as magnetic properties, stability, recyclability and peroxide-like properties (Song et al., 2020; Yi et al., 2020) have led to the synthesis of efficient composites of MoS_2 and Fe_3O_4 to use in many industrial applications. Previous researches have suggested that by loading Fe_3O_4 20 wt% nanoparticles on MoS_2 nanosheets lead to increase the activity of materials and can be recovered by extra magnetic (Zhang et al., 2017a; Lin et al., 2018; Song et al., 2018).

Design of experiments (DOE) is a systematic technique to define the relationships between variables influencing process and outputs. The basic idea of modern DOE is to alternate all variables at the same time over a set of designed experiments, then link and interpret the results via statistical models (Gabrielsson et al., 2002; Rahman and Raheem, 2023). Several advantages have been stated for DOE rather than traditional optimization method like OFAT (one factor at a time) (Weissman and Anderson, 2015; Karimifard and Moghaddam, 2018). Detection and considering the interactions between the chosen variables, extracting the maximum quantity of information using performance of the smallest amount of experiments, needing less laboratory work, being cost-effective in terms of time and money, finding reliable optimal conditions, divorcing the "noise'' of a reaction from actual agents and so on. Response surface methodology (RSM), among many DOE-based methods, has attracted attention in modeling, design of experiments, and optimization of different multivariate chemical processes (Rahman and Varshney, 2020).

This work aims to synthesize superparamagnetic $MoS_2/\gamma\text{-}Fe_2O_3$ nanocomposites (NCs) as efficient composites via various percentages of loaded $\gamma\text{-}Fe_2O_3$ (10, 20, and 30 %) nanoparticles (NPs) on the surface of 3D ball-flower-like MoS_2 that have been studied to remove Ni^{+2} and NO_3^- ions. The innovation of the present work the influence of the preparation parameters upon the catalytic performance of $MoS_2/\gamma\text{-}Fe_2O_3$ (10, 20, 30 %) catalyst was investigated using two procedures of usual experimental and RSM. In the first section, the removal of Ni^{+2} and

NO_3^- ions is examined by $MoS_2/\gamma\text{-}Fe_2O_3$ (10, 20, and 30 %) nanocomposites as efficient adsorption, and in the second section, using the experimental design in two steps. In order to identify the most effective synthesis parameters on the performance of nanocomposites, in the first step, modeling is performed based on the effect of four synthesis parameters such as temperature, amount of catalyst, and Ni^{+2} and NO_3^- ions concentrations on the adsorption capacity and removal percentage by response surface methodology (RSM) by historical data. Subsequently, the experimental design was carried out for independent variables of weight percent of $\gamma\text{-}Fe_2O_3$ nanoparticles, and species concentration using the central composite design (CCD). The designed experiments were conducted to determine the optimization process by design expert 7.0.0 software. The synthesized magnetic nanocomposites are prominently efficient, recyclable, economical, less energy-intensive, and easier to operate nanocomposites.

2. Experimental

The parts related to Materials and reagents, Synthesis of MoS_2 flower-like, Synthesis of $\gamma\text{-}Fe_2O_3$ Nanoparticles, and Nanocomposite characterization are mentioned in the supporting information file.

2.1. Synthesis of $MoS_2/\gamma\text{-}Fe_2O_3$ Nanocomposites

Superparamagnetic $MoS_2/\gamma\text{-}Fe_3O_4$ nanocomposites were also synthesized using the hydrothermal method for which various loading amounts of 10, 20, and 30 wt% $\gamma\text{-}Fe_2O_3$ in the samples were labeled as 10, 20, and 30 wt%- $MoS_2/\gamma\text{-}Fe_3O_4$, respectively. To synthesize (1 g) nanocomposite (10 wt%), the prepared $\gamma\text{-}Fe_3O_4$ (0.1 g) nanoparticles were weighed and added in 20 mL absolute ethanol to be probe-sonicated for 45 min. (2 mmol) $(NH_4)_6Mo_7O_{24}{\cdot}4H_2O$, and (4.5 mmol) H_2NCSNH_2 were dissolved in 50 mL deionized water to be stirred for 10 min. The solution was added to disperse $\gamma\text{-}Fe_3O_4$ nanoparticles, and the mixture was transferred into a stainless-steel autoclave after 30 min sonication and was heated for 24 h at 200 °C. Next, the prepared nanocomposites were separated by an external magnet and washed with deionized water several times, and dried in a vacuum at 60 °C for 12 h.

2.2. Adsorption experiments

At first, Stock solutions of 1 $mg.mL^{-1}$ Ni(II) and nitrate ions were purchased from Merck, and standard solutions were prepared by appropriate dilution with Milli-Q water. The adsorption experiments in 10 mL of aqueous solutions were conducted under consideration of pertinent factors such as ions concentration (0.1–0.5 M) Ni^{+2} and (0.1×10^{-4}-0.5×10^{-4} M) NO_3^-, temperature (25 and 50 °C), pH (4–9), and weight of catalyst (0.005 and 0.01 g). In the first section, the prepared suspensions were stirred for 1 h to study $MoS_2/\gamma\text{-}Fe_2O_3$ (10, 20, and 30 %) nanocomposites as efficient adsorptions. After the adsorption process, superparamagnetic nanocomposites were separated from the suspensions using an external magnet. The supernatant was determined by a UV–Vis–NIR spectrophotometer (Lambda 950, Perkin Elmer), and the spectra were recorded at the wavelength range of 250–800 nm. To reuse the catalyst after each step of absorption tests, the catalyst is collected and separated from the solution by an external magnet, then it is dried at 80 °C oven for overnight. It will be used several times.

Adsorption capacity at equilibrium (Qe, $mg.g^{-1}$) (Günay et al., 2007) and removal efficiency (Boulaiche et al., 2019) of heavy-metal Ni(II) and nitrate ions (%) were calculated via the following equations:

$$Qe = (C_0 - C_e)\frac{V}{m}$$

$$\text{Removal}\,(\%) = \frac{(C_0 - C_e)}{C_0} \times 100$$

Where C_0 and C_e ($mg.L^{-1}$) are the initial and equilibrium concentrations of heavy metals in the solution, respectively, V symbolizes the volume of mine water (L) taken for the adsorption study, and m denotes the weight (mg) of adsorption used.

2.3. Experimental design and central composite design (CCD)

The numerical optimization of processes employing RSM involves six sequential stages: (1) screening independent variables and choosing desired responses, (2) deciding on the experimental design strategy, (3) performing the designed experiments and collecting the experimental results, (4) obtaining the mathematical model correlating the input variables and responses, (5) fitting evaluation model via analysis of variance and diagnostic graphs, and (6) determination and validation of optimum circumstances (Yousefi et al., 2021; Haque et al., 2023; Rahman et al., 2023b). Central composite design (CCD) is recognized as the most popular response surface method (RSM) design. A CCD contains three groups of design points: (a) two-level factorial or fractional factorial design points, (b) axial/ star points, and (c) center points. The total number of experiments to execute in a CCD is obtained by the following formula:

$$N = 2^k + 2k + N_0 \tag{1}$$

Where k points to the number of variables and N0 reveals the number of replicates in the center point. The quadratic empirical model correlating response to input variables can be written by the following equation:

$$Y = b_0 + \sum_{i=1}^{n} b_i X_i + \sum_{i=1}^{n} b_{ii} X_i^2 + \sum_{i=1}^{n} \sum_{j)1}^{n} b_{ij} X_i X_j + \varepsilon \tag{2}$$

Where Y is the response function, Xi and Xj represent independent variables, b0 points to the intercept term, bi reveals the linear effect of Xi, bii signifies the quadratic effect of Xi, and bij means the two variable interactions between Xi and Xj.

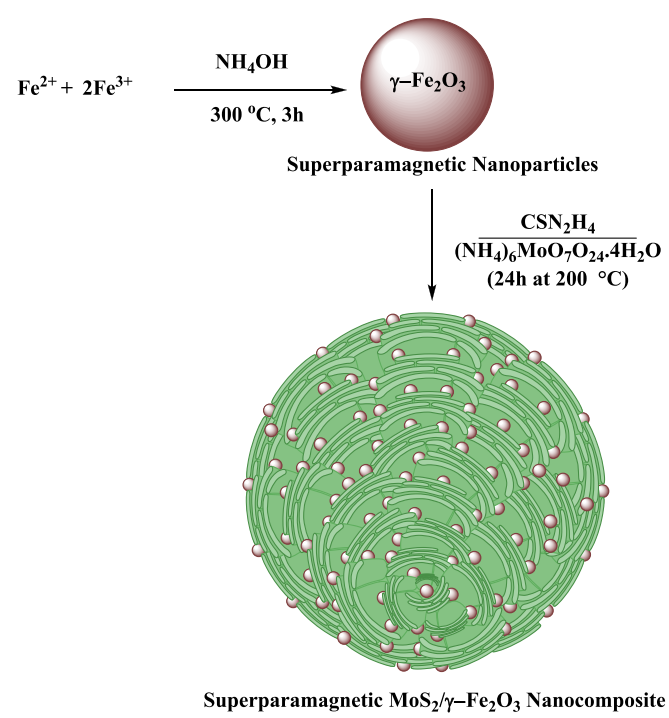

Fig. 1. Illustration for the synthesis procedure of superparamagnetic $MoS_2/\gamma\text{-}Fe_2O_3$ nanocomposite.

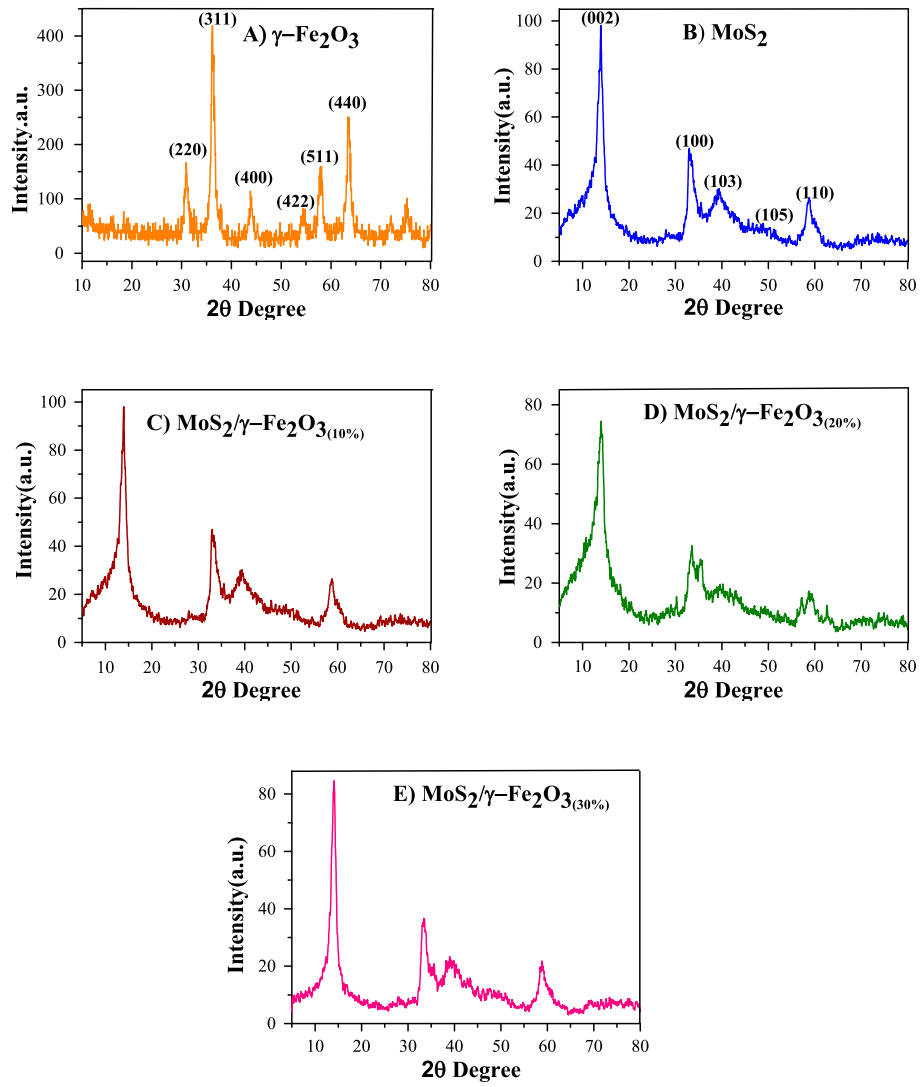

Fig. 2. XRD pattern of (A) γ-Fe_2O_3, (B) MoS_2, (C) MoS_2/γ-$Fe_2O_{3(10\%)}$, (D) MoS_2/γ-$Fe_2O_{3(20\%)}$, and (E) MoS_2/γ-$Fe_2O_{3(30\%)}$.

Table 1
Surface area, mean pore size and pore volume of γ-Fe_2O_3 NPs, MoS_2, and MoS_2/γ-$Fe_2O_{3(20\%)}$ nanocomposite.

Sample	S_{BET} [(a)] ($m^2.g^{-1}$)	D_{BJH} [(b)] (nm)	V_{BJH} [(c)] ($cm^3.g^{-1}$)
γ-Fe_2O_3	66.10	1.40	0.27
MoS_2	40.28	1.21	0.30
MoS_2/γ-$Fe_2O_{3(20\%)}$	47.06	1.64	0.35

(C) Total pore volume calculated by the Barret-Joyner-Halenda (BJH) equation.
[(a)] Specific surface area calculated by the Brunauer-Emmett-Teller equation (Sinha et al., 2019).
[(b)] Mean pore size diameter calculated by the Barret-Joyner-Halenda (BJH) equation (Bardestani et al., 2019).

3. 3.Result and discussion

The synthesis steps of the superparamagnetic nanocomposite with various percentages of loaded γ-Fe_2O_3 (10, 20, and 30 %) nanoparticles on flower-like MoS_2 are illustrated in Fig. 1. In the present study, MoS_2/γ-Fe_2O_3 nanocomposites are synthesized via the hydrothermal method as a recyclable catalyst for removing Ni^{+2} heavy metal and NO_3^- ions from the aquatic systems as efficient adsorptions using experimental design. The γ-Fe_2O_3 NPs were synthesized by a co-precipitation method and a mean crystal size of about 9.6 nm was verified by XRD analysis. The flower-like MoS_2 were employed as catalyst with high efficiency, and cost-effective to prepare nanocomposites by in situ growth of γ-Fe_2O_3 nanoparticles on the surfaces of flower-like MoS_2. In this study, the design of experiments was used in two steps as follows:

In the first part, using response surface methodology (RSM) models for the Qe and removal percent are created. The influence of process variables, including the concentration of Ni^{+2} and NO_3^-, the weight of the catalyst, and reaction temperature have been studied; and in the following, effective variables were detected. In the second part, using the central composite design (CCD), the experimental design is performed for three independent variables of weight percent of γ-Fe_2O_3, kind of removed species, and species concentration. Finally, the identified optimal conditions are confirmed aiming at maximizing Qe and removal percent.

The XRD spectra of γ-Fe_2O_3 NPs, flower-like MoS_2, and MoS_2/γ-Fe_2O_3 NCs are shown in Fig. 2. Diffraction peaks at 2θ = 30.3°, 35.7°, 43.2°, 53.3°, 56.9° and 62.8° pertain to the crystal planes 220, 311, 400, 422, 511 and 440 of the magnetite structure (JCPDS no. 04–0755) of the cubic lattice of γ-Fe_2O_3 NPs, respectively (Fig. 2A). Applying the XRD analysis, employing the Debye-Scherrer equation to calculate the full width at half-height of the 311 reflection peak at 35.7° (2θ) the mean crystallite size was obtained in the range of 9.5–9.7 nm (Ostovar et al., 2019; Saberi et al., 2020). Diffraction peaks at 2θ = 13.8°, 33.4°, 39.2°, 49.4° and 58.9° could be indexed to (0 0 2), (1 0 0), (1 0 3), (1 0 5), and

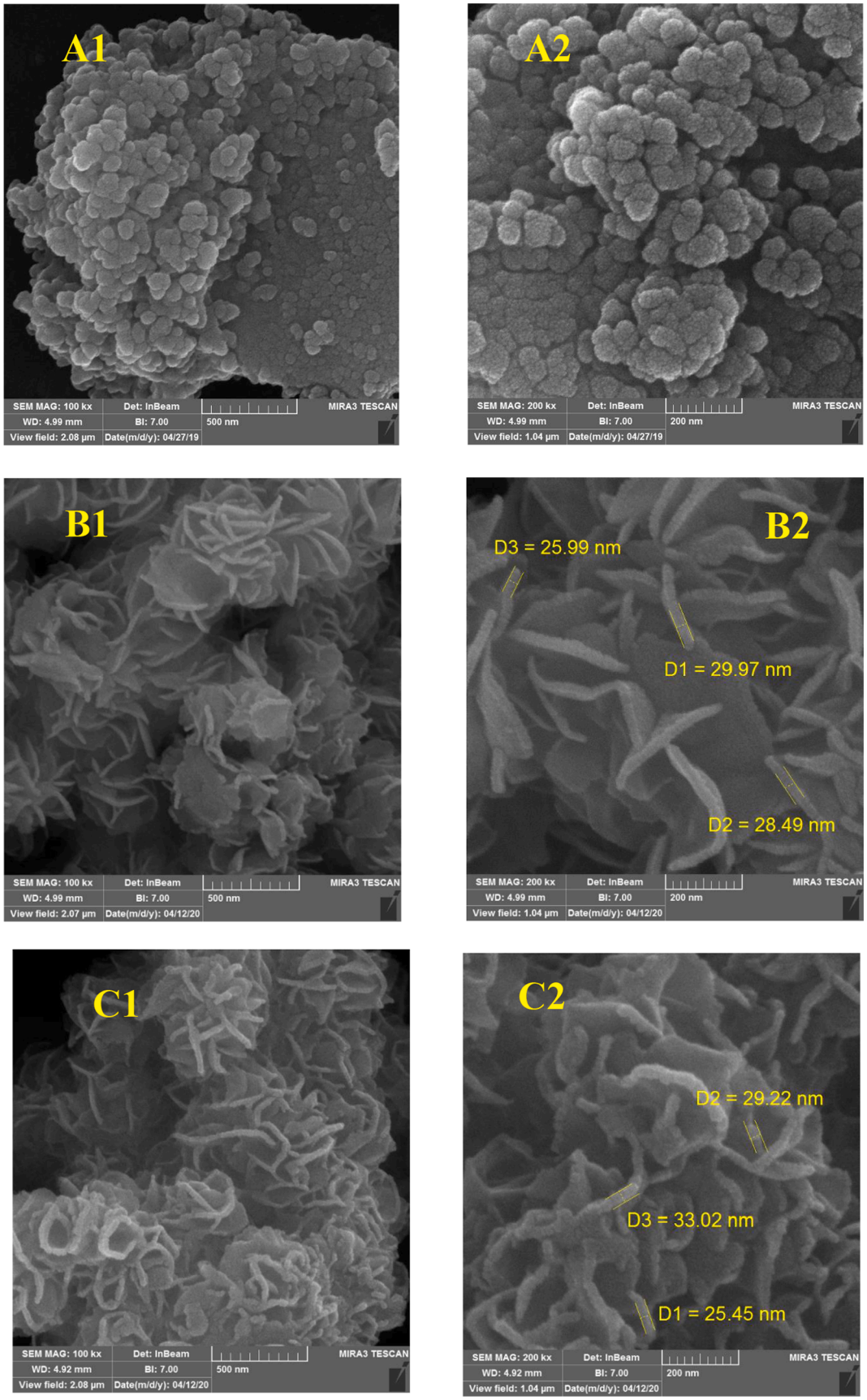

Fig. 3. SEM images of (A1-2) γ-Fe_2O_3, (B1-2) MoS_2, and (C1-2) MoS_2/γ-$Fe_2O_{3(20\%)}$ nanocomposite.

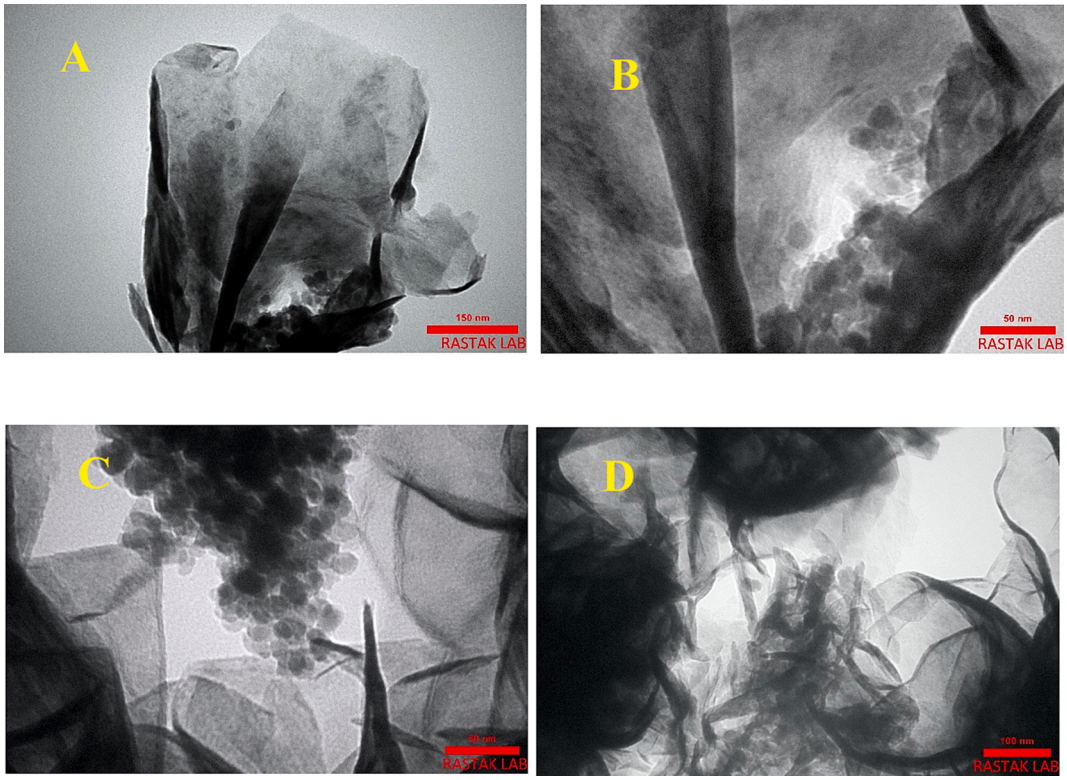

Fig. 4. TEM images of $MoS_2/\gamma\text{-}Fe_2O_{3(20\%)}$ nanocomposite.

(1 1 0) planes of MoS_2 structure (JCPDS no. 37–1492), respectively (Fig. 2B). The strong peak reflections with the very sharp and high intensity of the (0 0 2) plane are clearly visible that confirms the well-stacked crystalline structure and the structural nature of the flower-like MoS_2 (Hu et al., 2014; Kumar et al., 2017; Jing Liu et al., 2019). Diffraction peaks at $2\theta = 13.8°$, 33.4°, 35.7°, 39.2°, 43.2°, 56.9°, 58.9°, and 62.8° are observed for the synthesized nanocomposites (Fig. 2C-E). Comparison of the $MoS_2/\gamma\text{-}Fe_2O_3$ nanocomposites with $\gamma\text{-}Fe_2O_3$ NPs and MoS_2 patterns suggest that MoS_2 synthesized was high crystallinity and larger particles and their scattering angle is more than that of pure flower-like MoS_2, which may be due to the stable structure of $MoS_2/\gamma\text{-}Fe_2O_3$. The characteristic peaks of nanocomposite in the XRD pattern is illustrated to match well with those of $\gamma\text{-}Fe_2O_3$ Nps and MoS_2 patterns, which could confirm that magnetic $\gamma\text{-}Fe_2O_3$ NPs are successfully loaded on the surface of flower-like MoS_2 and thus the XRD pattern of nanocomposite demonstrates nanocomposite (Han et al., 2017; Bagheri and Chaibakhsh, 2020; He et al., 2020).

N_2 adsorption–desorption isotherm and pore-size distributions (BJH, desorption branch) of $\gamma\text{-}Fe_2O_3$ NPs, MoS_2, and $MoS_2/\gamma\text{-}Fe_2O_{3(20\%)}$ nanocomposites are demonstrated in Fig. S1. All of the samples provide type IV isotherms and type H3 hysteresis loops that confirm mesoporous structures of the as-synthesized samples. The specific surface area and pore volume of the $MoS_2/\gamma\text{-}Fe_2O_{3(20\%)}$ nanocomposites show 47.06 $m^2.g^{-1}$, and 0.35 $cm^3.g^{-1}$, respectively (Table 1). The high special surface area and increased porosity of nanocomposites lead to increasing active sites to improve the reaction capacity of the substance. (Gao et al., 2016; Chaocheng Li et al., 2017; Mu et al., 2018).

Fig. 3 displays the nanoparticles' morphology of the as-synthesized $\gamma\text{-}Fe_2O_3$ NPs, flower-like MoS_2, and $MoS_2/\gamma\text{-}Fe_2O_{3(20\%)}$ NCs in the form of a flower-like morphology that is in agreement with the TEM analysis (Fig. 4). Detailed observation of SEM images of both $MoS_2/\gamma\text{-}Fe_2O_{3(10\%)}$, and $MoS_2/\gamma\text{-}Fe_2O_{3(30\%)}$ reveal the morphology of flower-like in Fig. S2. The morphology of the $MoS_2/\gamma\text{-}Fe_2O_3$ nanocomposite demonstrates a regular surface, and the morphology of the flower-like MoS_2 is maintained after the addition of $\gamma\text{-}Fe_2O_3$ nanoparticles. The elemental mapping analysis (Fig. S3) and EDX spectra (Fig. S4, Table S1) include the elements of O, Fe, S, and Mo that confirm the successful formation of the $\gamma\text{-}Fe_2O_3$ NPs with uniform distribution on $MoS_2/\gamma\text{-}Fe_2O_3$ surface. The masses of $\gamma\text{-}Fe_2O_3$ NPs and flower-like MoS_2 were analyzed by ICP-MS and the amount of flower-like MoS_2 was calculated to about 43.7 % (Table S1). The transmission electron microscopy TEM image of the $MoS_2/\gamma\text{-}Fe_2O_{3(20\%)}$ nanocomposite was carried out to examine a sheet-like structure of the nanocomposite, and some well-dispersed $\gamma\text{-}Fe_2O_3$ NPs loading on the surface of flower-like MoS_2 can be seen clearly in Fig. 4. To indicate high thermal stability of MoS_2 and $MoS_2/\gamma\text{-}Fe_2O_{3(20\%)}$ nanocomposite, the thermogravimetric analysis (TGA) was carried out, showing mass loss during heating from room temperature to 800 °C in Fig. S5. For both samples, weight loss below 150 °C was observed, which may be due to the vaporization of the adsorbed water and solvent molecules. The total weight loss of MoS_2 and $MoS_2/\gamma\text{-}Fe_2O_{3(20\%)}$ nanocomposite was 5.1 and 8 (wt%) at 620 and 700 °C, respectively. According to reported literature, the heating process MoS_2 can lead to the production of molybdenum oxide and Sulfur dioxide (SO_2) (Jing Li et al., 2014; Gao et al., 2016; Kumar et al., 2017).

The $\gamma\text{-}Fe_2O_3$ NPs, MoS_2, and $MoS_2/\gamma\text{-}Fe_2O_3$ nanocomposites were examined by FTIR spectroscopy, and the FTIR spectra are depicted in Fig. S6. The FTIR spectra of MoS_2 and $MoS_2/\gamma\text{-}Fe_2O_3$ nanocomposites showed a very strong characteristic stretching vibration peak of Mo-S around 600 cm^{-1} that confirmed the presence of MoS_2 at those composites. Absorption peaks around 575 cm^{-1} are assigned to the Fe-O in $\gamma\text{-}Fe_2O_3$ NPs, indicating the successful preparation of $\gamma\text{-}Fe_2O_3$ NPs formed on the surface of $MoS_2/\gamma\text{-}Fe_2O_3$ nanocomposites (Ma and Row, 2020). The magnetic properties of $\gamma\text{-}Fe_2O_3$ NPs and $MoS_2/\gamma\text{-}Fe_2O_3$ nanocomposites were carried out to examine by VSM at an ambient temperature (300 K) in the range of −10000 to 10,000 G. Field-dependent magnetization curves of bare $\gamma\text{-}Fe_2O_3$ NPs and $MoS_2/\gamma\text{-}Fe_2O_3$ nanocomposites are depicted in Fig. S7. The saturation magnetization (Nayak et al., 2011) value of $\gamma\text{-}Fe_2O_3$ NPs and $MoS_2/\gamma\text{-}Fe_2O_3$ nanocomposites were found to be 67.2 and 44.6 $emu.g^{-1}$ identified as superparamagnetic.

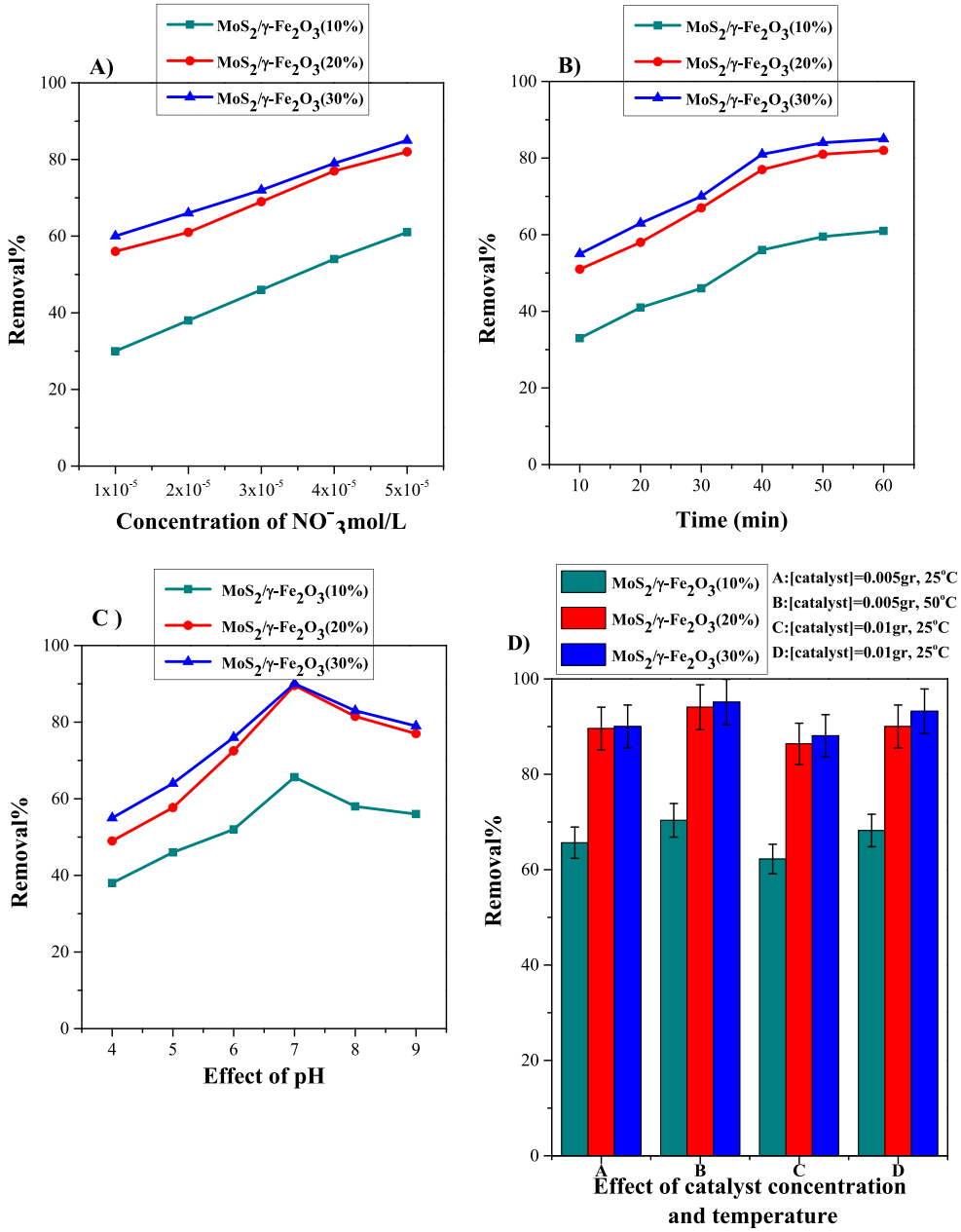

Fig. 5. The effect of different (A) NO_3^- concentration ([catalyst] = 0.005 g, temperature = 25 °C, time = 60 min), (B) Time ([NO_3^-] = 0.5 × 10^{-4}M, [catalyst] = 0.005 g, temperature = 25 °C), (C) pH ([NO_3^-] = 0.5 × 10^{-4}M, [catalyst] = 0.005 g, temperature = 25 °C, time = 50 min), (D) catalyst concentration and temperature ([NO_3^-] = 0.5 × 10^{-4}M, pH = 7, time = 50 min).

3.1. Study of adsorption tests

The three superparamagnetic $MoS_2/\gamma\text{-}Fe_2O_3$ (10, 20, and 30 %) nanocomposites as an efficient adsorption were studied to eliminate of heavy metal Ni^{+2} and NO_3^- ions for environmental remediation as efficient adsorption. The individual removal of both solutions contains Ni^{+2} and NO_3^- ions by optimizing the concentration of catalysts and ions, amount of loading $\gamma\text{-}Fe_2O_3$ nanoparticle, pH, reaction time, and reaction temperature to evaluate the performance of catalysts. The catalytic tests were examined taking into account factors such as ions concentration (0.1–0.5 mol.L^{-1}) Ni^{+2} and (0.1 × 10^{-4}-0.5 × 10^{-4} mol.L^{-1}) NO_3^-, Time (10–60 min), pH (4–9), the weight of catalyst (0.005 and 0.01 g), percentage of loaded $\gamma\text{-}Fe_2O_3$ nanoparticles (10, 20, and 30 %), and temperature (25 and 50 °C).

The adsorption experiments were performed to optimize the ions concentration at ambient temperature in the presence of 0.005 g nanocomposites for 60 min, which was reported as 0.5 × 10^{-4} mol.L^{-1} and 0.5 mol.L^{-1} as the optimized concentration for NO_3^- (Fig. 5A) and Ni^{+2} (Fig. 6A) ions, respectively. In the continuance of the optimization process, the absorption process was examined every ten min, and the optimized time was obtained from the highest percentage of NO_3^- (Fig. 5B) and Ni^{+2} (Fig. 6B) ions removal, respectively, 50 and 40 min. The optimization pH was received at about pH = 7 for NO_3^- ion (Fig. 5C) and pH = 8 for Ni^{+2} ion(Fig. 6C).

In Fig. S8, the point charges of zero (pH_{pzc}) of $MoS_2/\gamma\text{-}Fe_2O_{3(20\%)}$ NPs based on initial pH and final pH are indicated at about 7.5 point. Point zero charge is known as the characteristic pH value at which the surface charge of a material becomes zero. It means that all active sites on the surface are neutral (Al-Maliky et al., 2021). When the pH value of the solution is higher than the PZC point, it means that the charge on the

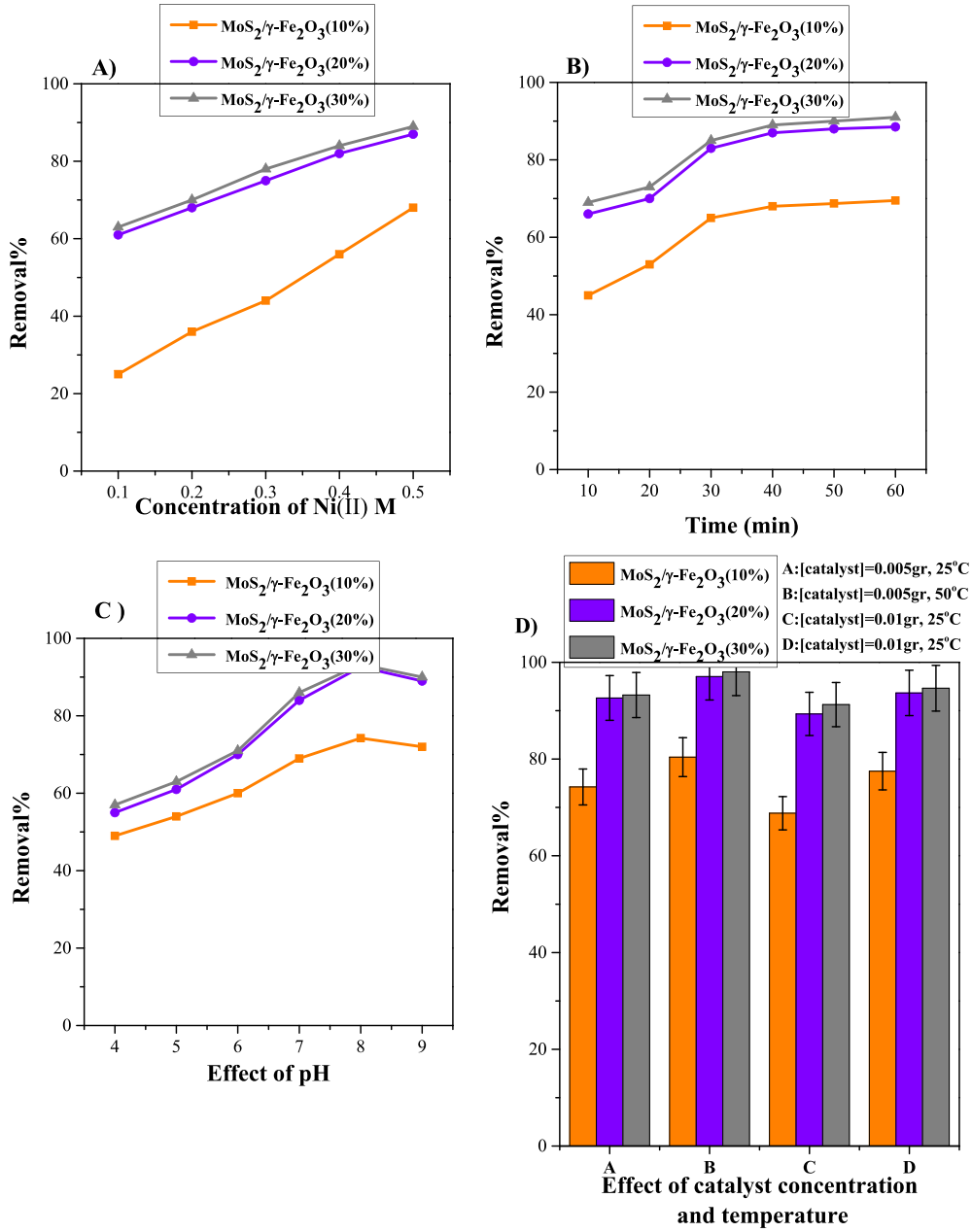

Fig. 6. The effect of different (A) Ni + 2 concentration ([catalyst] = 0.005 g, temperature = 25 °C, time = 60 min), (B) Time ([Ni + 2] = 0.5 M, [catalyst] = 0.005 g, temperature = 25 °C), (C) pH ([Ni + 2] = 0.5 M, [catalyst] = 0.005 g, temperature = 25 °C, time = 40 min), (D) catalyst concentration and temperature ([Ni + 2] = 0.5 M, pH = 8, time = 40 min).

nanoparticle surface is negative and leads to the adsorption of positively charged pollutants. Therefore, by increasing of solution pH (pH = 8), the surface of $MoS_2/\gamma\text{-}Fe_2O_{3(20\%)}$ NPs has negative charges, and the interaction between the surface of the nanoparticle and Ni^{+2} ion increases, resulting in a significant increase in Ni^{+2} uptake. On the contrary, for pH lower than the PZC point, the surface of the composite is positive and has absorbed polluting cations. The pH of the optimized solution for NO_3^- ion removal has been reported to be at pH = 7, which is lower than the PZC point of the composite and indicates the positive charges on the surface and the absorption of nitrate ions (GUILHEN et al., 2022). The concentration of nanocomposites and process temperature value were optimized that was shown maximum removal of both ions by 0.005 g nanocomposites at 50 °C (Fig. 5D, 6D).

The subsequent experiments to determine adsorption capacity (Qe) and removal efficiency were carried out only with optimized parameters: i) in Fig. 7A, B for (0.5×10^{-4} mol.L^{-1}) NO_3^-, pH = 7, time = 50 min, temperature = 50 °C, 0.005 g catalyst, ii) in Fig. 7C, D for (0.5 mol.L^{-1}) Ni^{+2} pH = 8, time = 40 min, temperature = 50 °C, 0.005 g catalyst. Fig. 7 shows adsorption capacity and removal for catalyst based on the concentration of both ions. In order to remove Ni^{+2} and NO_3^- ions in the presence of the $MoS_2/\gamma\text{-}Fe_2O_3$ (10 %) catalyst compared to other $MoS_2/\gamma\text{-}Fe_2O_3$(20 %-30 %) catalysts do not have well-shown results that due to the low percentage of magnetic nanoparticles were led to the low efficiency of nanocomposites. The higher adsorption capacity (Qe) and removal efficiency of NO_3^- (0.5×10^{-4} M) and Ni^{+2} (0.5 M) ions are achieved 9.4×10^{-5} mg/g, 94 %, 0.97 mg/g, and 97 %, respectively, using 0.005 g $MoS_2/\gamma\text{-}Fe_2O_{3(20\%)}$ nanocomposite at 50 °C.

To evaluate the stability and reusability of the nanocomposite (loaded of $\gamma\text{-}Fe_2O_3$ 20 % percentage) were used as adsorption in successive experiments (Fig. 7E). The heavy metal Ni^{+2} ions were

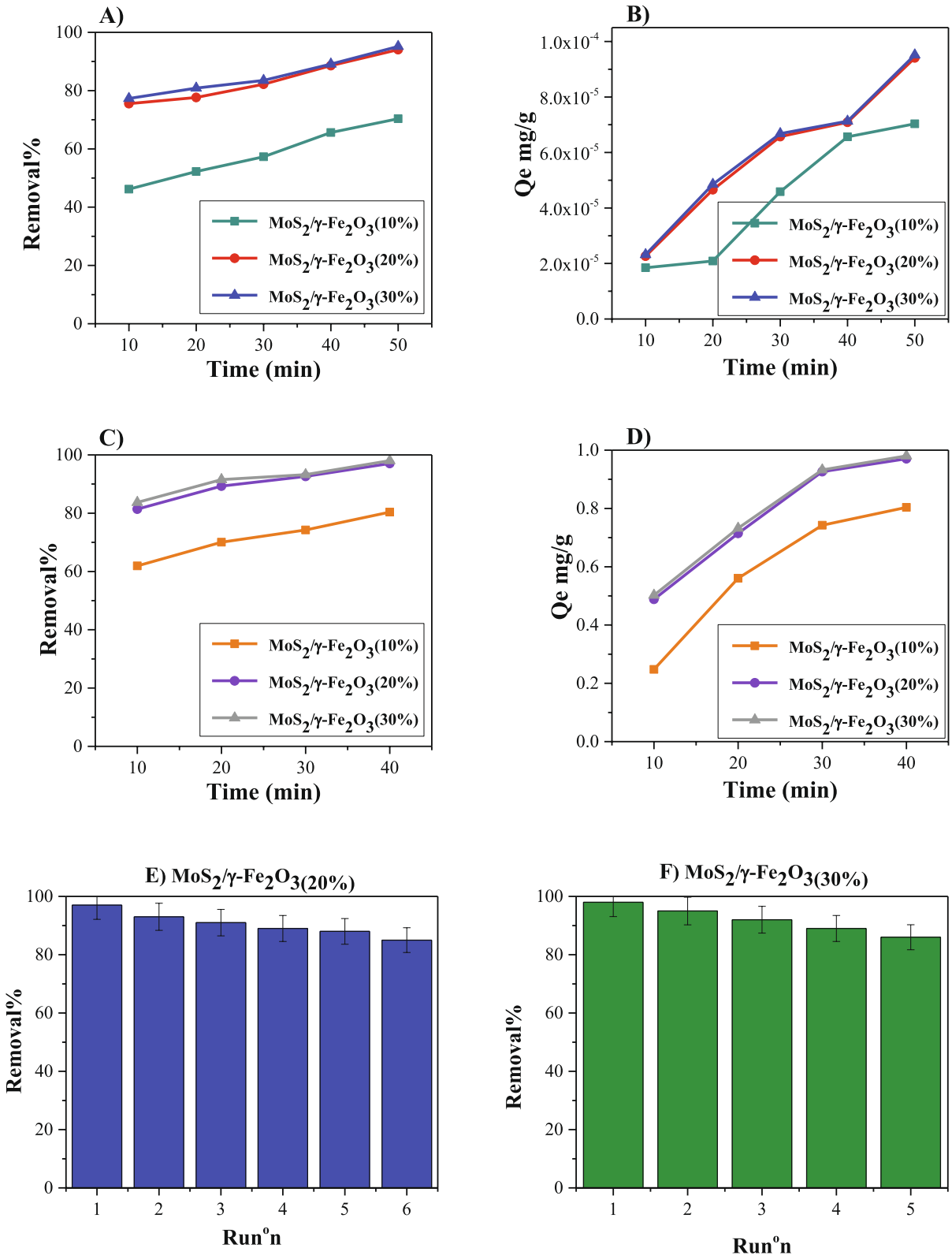

Fig. 7. (A) Removal efficiency for NO_3^- ion, (B) Adsorption capacity for NO_3^- ion, (C) Removal efficiency for Ni^{+2} ion, and (D) Adsorption capacity for Ni^{+2} ion (under condition for A, B. ($[NO_3^-] = 0.5 \times 10^{-4}$ M, [catalyst] = 0.005 g, temperature = 50 °C, pH = 7, time = 50 min), and for C, D. $[Ni^{+2}]$ = 0.5 M, [catalyst] = 0.005 g, temperature = 50 °C, pH = 8, time = 40 min), Reusability of (E) the MoS2/γ-Fe2O3(20 %) nanocomposite and (F) the MoS2/γ-Fe2O3(30 %) nanocomposite to remove Ni^{+2} ions after 6th cycle.

Table 2
List of actual and coded variables, and corresponding experimental ranges used for modeling.

Actual variables	Unit	Type	Symbol	Low actual	High actual
Ni^{2+} Concentration	mol/L	Numeric	Ni^{2+} Conc.	0.1	0.5
NO_3^- Concentration	mol/L	Numeric	NO_3^- Conc.	0.1×10^{-4}	0.5×10^{-4}
Weight of adsorbent	g	Numeric	Cat.	5.000E-003	1.000E-002
Temperature	°C	Numeric	T	25.00	50.00

Table 3
ANOVA table of Qe and removal percent of $MoS_2/\gamma\text{-}Fe_2O_3$ nanocomposites.

Nanocomposites	Model	F-value	p-value	Std.Dev	R^2	adj-R^2	Pred-R^2	adequate precision
$MoS_2/\gamma\text{-}Fe_2O_3$(10 %) Ni^{+2}	Qe	639.91	< 0.0001	0.018	0.9956	0.9941	0.9902	78.601
	Removal	604.34	< 0.0001	1.67	0.9913	0.9896	0.9870	74.524
$MoS_2/\gamma\text{-}Fe_2O_3$(10 %)$NO_3^-$	Qe	1278.67	< 0.0001	9.922E-007	0.9983	0.9975	0.9953	112.810
	Removal	2511.51	< 0.0001	0.64	0.9979	0.9975	0.9966	151.735
$MoS_2/\gamma\text{-}Fe_2O_3$(20 %) Ni^{+2}	Qe	2386.85	< 0.0001	0.011	0.9988	0.9984	0.9974	151.770
	Removal	355.39	< 0.0001	1.25	0.9896	0.9868	0.9813	60.140
$MoS_2/\gamma\text{-}Fe_2O_3$(20 %)$NO_3^-$	Qe	1605.22	< 0.0001	1.280E-006	0.9983	0.9976	0.9961	124.101
	Removal	603.96	< 0.0001	1.16	0.9912	0.9896	0.9871	75.405
$MoS_2/\gamma\text{-}Fe_2O_3$(30 %) Ni^{+2}	Qe	2517.80	< 0.0001	0.011	0.9989	0.9985	0.9975	155.892
	Removal	257.50	< 0.0001	1.47	0.9856	0.9818	0.9750	50.837
$MoS_2/\gamma\text{-}Fe_2O_3$(30 %)$NO_3^-$	Qe	2688.93	< 0.0001	8.417E-007	0.9994	0.9990	0.9977	164.910
	Removal	1383.08	< 0.0001	0.64	0.9973	0.9966	0.9954	115.973

Table 4
CCD design summary.

Name	Symbol	Unit	Type	Low actual	High actual
weight percent of $\gamma\text{-}Fe_2O_3$	$\gamma\text{-}Fe_2O_3$	%	Numeric	10.00	30.00
NO_3^- concentration ($\times 10^{-4}$)	Conc. ($\times 10^{-4}$)	mol. L^{-1}	Numeric	0.10	0.50
Ni^{+2} concentration	Conc.	mol. L^{-1}	Numeric	0.10	0.50

successfully removed in solution and obtained the same result for $MoS_2/\gamma\text{-}Fe_2O_3$(30 %) nanocomposite after six repeated runs (Fig. 7F). To study the structural stability of recycled nanocomposites, is considered using SEM and FTIR analysis after the four successive runs that no obvious change is be observed (Fig. S9).

Several researches have been executed on the mechanism of heavy metal adsorption on MoS_2 nanosheets. Z. Wang and his colleagues (Wang et al., 2018) have associated the mechanism for Hg^{2+} adsorption on MoS_2 nanosheets through ion exchange between Hg^{2+} and cations (e.g., H^+) on the MoS_2 surface. In addition, it has been demonstrated that Hg^{2+} can be adsorbed on MoS_2 surface in the form of multilayers, where the adsorption of the first layer is attributed to the complexation of Hg^{2+} with S atoms while the adsorption of subsequent layers mainly results from electrostatic interaction (Wang et al., 2018). In addition, M.J. Aghagoli, et al have stated that the adsorption of Ni(II) ions on MoS_2 is mainly due to the electrostatic interaction of ions on molybdenum disulfide surface (AghagoliShemirani, 2017). To study the adsorption of MoS2-based catalysts, the comparison Table S21 is reported. In the next section, we investigated the adsorptions nanocomposites by using experimental design approach in two parts as follows:

3.2. The experimental design Approach

3.2.1. The experimental design Approach: Part I: Detection of significant parameters on Qe and removal percent responses of different nanocompposites

In this section, in the first step, the modeling of the effect of independent synthesis conditions on the Qe and removal percent of the various percentages of superparamagnetic nanocomposites has been considered using response surface methodology (RSM) and historical data. Consequently, with regard to developed mathematical models and coefficient estimations of different terms, the most effective variables were detected. Here, the superparamagnetic nanocomposites comprise $MoS_2/\gamma\text{-}Fe_2O_{3(10\%)}$, $MoS_2/\gamma\text{-}Fe_2O_{3(20\%)}$, and $MoS_2/\gamma\text{-}Fe_2O_{3(30\%)}$, and the four input variables contain a concentration of Ni^{+2} and NO_3^- ions, the weight of the catalyst, and reaction temperature. The four considered independent variables, symbols, and experimental ranges are summarized in Table 2, which is reported all obtained experimental results in Figs. S10, and 11. The used experimental data and obtained responses for the three superparamagnetic nanocomposites were tabulated in Tables S2-4. The modeling study and assessment of the prominence of individual/binary impacts of synthesis variables on responses, ANOVA, and optimization were performed by response surface and design expert 7.0.0 software.

In order to depict the mathematical relationships between independent variables and response values, empirical models were obtained via the least square of error. If the fitted model developed by the least square regression has an adequate estimation of experimental results, it can be employed to evaluate the real system (Akbari et al., 2019; Mirzaei et al., 2021). As illustrated in Equation (2), the general quadratic models cover linear (A, B, C and, D), interaction (A × B, A × C, A × D, B × C, B × D, and C × D) and squared terms (A^2, B^2, C^2, and D^2) of independent variables applied to predict the influence of independent variables on response behavior. The empirical data from Tables S2-4 were employed to generate second-order quadratic equations. After taking out the insignificant terms with regard to p-values on ANOVA, the final reduced quadratic equations in terms of coded variables for sufficiently forecasting Qe and removal percent were created as follows (Equations (3)-(14)):

$MoS_2/\gamma\text{-}Fe_2O_{3(10\%)}$: Ni^{+2}

$$Qe = +0.24 + 0.26A - 0.10B + 0.017C - 0.092AB + 0.068A^2 \quad (3)$$

$MoS_2/\gamma\text{-}Fe_2O_{3(10\%)}$: Ni^{+2}

$$Removal = +52.34 + 21.60A - 2.45B + 3.85C \quad (4)$$

$MoS_2/\gamma\text{-}Fe_2O_{3(10\%)}$:$NO_3^-$

$$Qe = +(2.268E-005) + (2.265E-005)A - (9.104E-006)B + (1.351E-006)C - (7.959E-006)AB + (7.922E-007)AC + (4.977E-006)A^2 \quad (5)$$

$MoS_2/\gamma\text{-}Fe_2O_{3(10\%)}$:$NO_3^-$

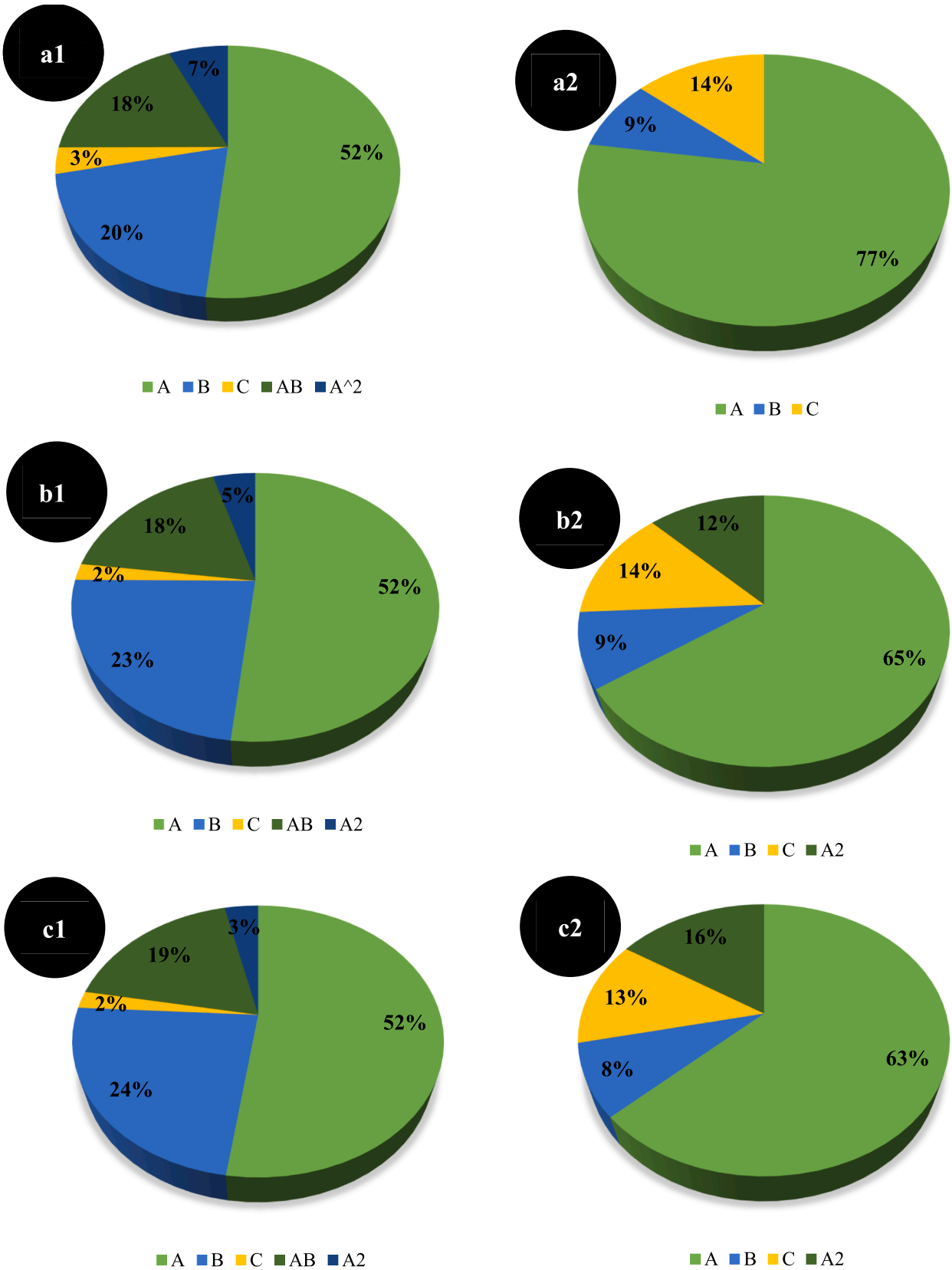

Fig. 8. Percent contribution of different terms upon (1) Qe and (2) removal percent, for $MoS_2/\gamma\text{-}Fe_2O_{3(10\%)}$ (a), $MoS_2/\gamma\text{-}Fe_2O_{3(20\%)}$ (b) and $MoS_2/\gamma\text{-}Fe_2O_{3(30\%)}$ (c) nanocomposites (A. Ni^{+2} concentration, B. weight of the nanocomposites, and C. reaction temperature.

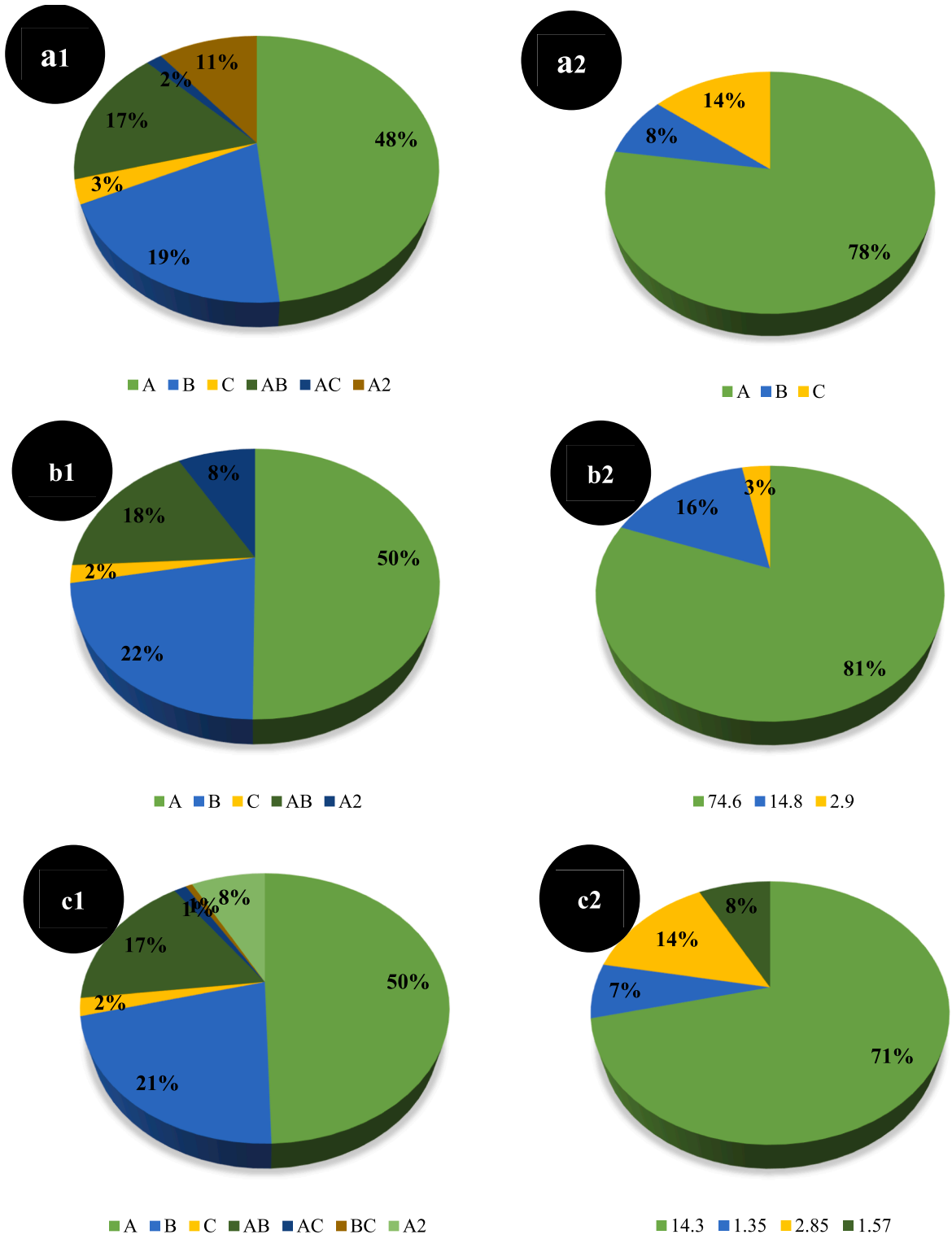

Fig. 9. Percent contribution of different terms upon (1) Qe and (2) removal percent, for $MoS_2/\gamma\text{-}Fe_2O_{3(10\%)}$ (a), $MoS_2/\gamma\text{-}Fe_2O_{3(20\%)}$ (b) and $MoS_2/\gamma\text{-}Fe_2O_{3(30\%)}$ (c) nanocomposites (A. NO_3^- concentration, B. weight of the nanocomposites, and C. reaction temperature.

$$Removal = +49.40 + 16.85A - 1.80B + 3.10C \quad (6)$$

$MoS_2/\gamma\text{-}Fe_2O_{3(20\%)}$: Ni^{+2}

$$Qe = +0.37 + 0.31A - 0.14B + 0.012C - 0.11AB + 0.027A^2 \quad (7)$$

$MoS_2/\gamma\text{-}Fe_2O_{3(20\%)}$: Ni^{+2}

$$Removal = +82.02 + 13.95A - 1.90B + 2.90C - 2.64A^2 \quad (8)$$

$MoS_2/\gamma\text{-}Fe_2O_{3(20\%)}$:$NO_3^-$

$$Qe = +(3.385E-005) + (2.945E-005)A - (1.281E-005)B + (1.240E-006)C - (1.040E-005)AB + (4.819E-006)A^2 \quad (9)$$

Table 5
The central composite design of independent variables and related laboratory responses.

(a) Run	A γ-Fe_2O_3 (%)	B NO_3^- concentration (×10^{-4}) (mol/L)	Qe (mg/g)	removal (%)
1	20.00	0.10	1.3008E-005	65
2	10.00	0.30	3.33365E-005	55
3	20.00	0.30	4.65934E-005	77
4	20.00	0.50	9.40771E-005	94
5	20.00	0.30	5.05934E-005	76
6	30.00	0.30	4.85178E-005	80
7	10.00	0.10	7.44868E-006	37
8	30.00	0.50	9.51463E-005	95
9	20.00	0.30	4.25934E-005	78
10	20.00	0.30	4.85934E-005	76
11	10.00	0.50	7.0343E-005	70
12	30.00	0.10	1.34357E-005	67
13	20.00	0.30	4.70934E-005	77
(b) Run	**A γ-Fe_2O_3 (%)**	**B Ni^{+2}concentration (mol/L)**	**Qe (mg/g)**	**removal (%)**
14	20.00	0.50	0.970531	97
15	10.00	0.10	0.0743961	37
16	20.00	0.30	0.5244	87
17	30.00	0.10	0.142754	71
18	10.00	0.50	0.803865	80
19	30.00	0.50	0.980193	98
20	20.00	0.30	0.5951	89
21	10.00	0.30	0.355556	59
22	20.00	0.30	0.5048	86
23	20.00	0.30	0.625	90
24	20.00	0.10	0.14058	70
25	30.00	0.30	0.543961	90
26	20.00	0.30	0.524638	87

$MoS_2/\gamma\text{-}Fe_2O_{3(20\%)}$:$NO_3^-$

$$Removal = +74.60 + 14.80A - 1.80B + 2.90C \quad (10)$$

$MoS_2/\gamma\text{-}Fe_2O_{3(30\%)}$: Ni^{+2}

$$Qe = +0.39 + 0.31A - 0.14B + 0.012C - 0.11AB + 0.021A^2 \quad (11)$$

$MoS_2/\gamma\text{-}Fe_2O_{3(30\%)}$: Ni^{+2}

$$Removal = +84.05 + 13.95A - 1.90B + 2.80C - 3.50A^2 \quad (12)$$

$MoS_2/\gamma\text{-}Fe_2O_{3(30\%)}$:$NO_3^-$

$$Qe = +(3.464E-005) + (2.974E-005)A - (1.288E-005)B + (1.270E-006)C - (1.025E-005)AB + (7.922E-007)AC - (4.207E-007)BC + (4.699E-006)A^2 \quad (13)$$

$MoS_2/\gamma\text{-}Fe_2O_{3(30\%)}$:$NO_3^-$

$$Removal = +75.86 + 14.30A - 1.35B + 2.85C + 1.57A^2 \quad (14)$$

With regard to developed equations, parameter A has a positive effect on whole responses (Qe and removal percent) for all weight percent of γ-Fe_2O_3. In other word, with an increase in parameter A (concentration of Ni^{+2} or NO_3^-), Qe and removal percent responses increased. In the following, parameter B (weight of catalyst) has a negative influence in both responses of Qe and removal percent and for all weight percent of γ-Fe_2O_3, as found from negative coefficient. With the decrease in weight of catalyst, Qe and removal percent responses increased. An increase in parameter C (reaction temperature) led to an increase in Qe and removal percent, due to a positive coefficient. Regarding obtained equations, the maximum influence of parameters belong to Ni^{+2} and NO_3^- concentrations, because of their high coefficients. It is worth mentioning in the final obtained equations, some interaction and binary terms have been omitted, because of their minimal effect on the model (recognized by their high p-values (greater than 0.05)).

The statistical importance of the created quadratic models was assessed using analysis of variance (ANOVA). This includes a full analysis of variance, prediction equations, and case statistics comprising F-value, p-value < 0.05, predicted R^2, R^2, adjusted R^2, and adequate precision. In order to assess the acceptability of the model, the diagnostic schemes were considered, too. The R^2 value is improved by omitting and adding some terms in the equation.

The ANOVA analysis for developed quadratic models were illustrated in Tables S5-S16 and summarized in Table 3.

Model F-value and related probability value (p-value) are used to approve model significance. In plain language, if the p-value is less than 0.05, then the model or terms in the model have a significant effect on the response. The small values of model p-values (<0.0001) confirmed the accuracy and reliability of the developed model.

R^2 is a measure of the amount of variation about the mean illuminated by the model. Adjusted R^2 is a measure of the amount of deviation about the mean illuminated by the model and adjusted for the number of terms in it. In better words, if the number of unimportant terms in the model increases, the adjusted R^2 decreases. Therefore, adjusted R^2 is a more unbiased statistical parameter rather than R^2. High values of the R^2 and adjusted R^2 (higher than 0.95) for whole responses (Table 3) revealed suitable fitting of the experimental data. Predicted R^2 is a measure of the amount of variation in new data enlightened by the model. The difference between predicted R^2 and adjusted R^2 should be less than 0.20. If not, there may be a problem with either the model or data. The very small differences between adjusted R^2 and predicted R^2 (<0.2) for all responses proved the perfect prediction of developed models.

Adequate precision compares the span of the predicted values at the design space with the average prediction error, and hence is a signal-to-noise ratio. Values more than 4 point to acceptable model discrimination. As presented in Table 3, all responses showed adequate precision.

The statistical validation and goodness of the fitting of developed models could be graphically scanned using the diagnostics plots, too. Most of the plots demonstrating residuals express how well the model satisfies the assumptions of the analysis of variance. According to Figs. S12-S17 (a1 and a2) for Qe and removal percent of different nanocomposites, a normal scattering of residuals close a straight line, with no specific arrangements, approves that the residuals tail a normal distribution. The residuals versus predicted plot demonstrate the residuals versus the rising predicted response values and check the

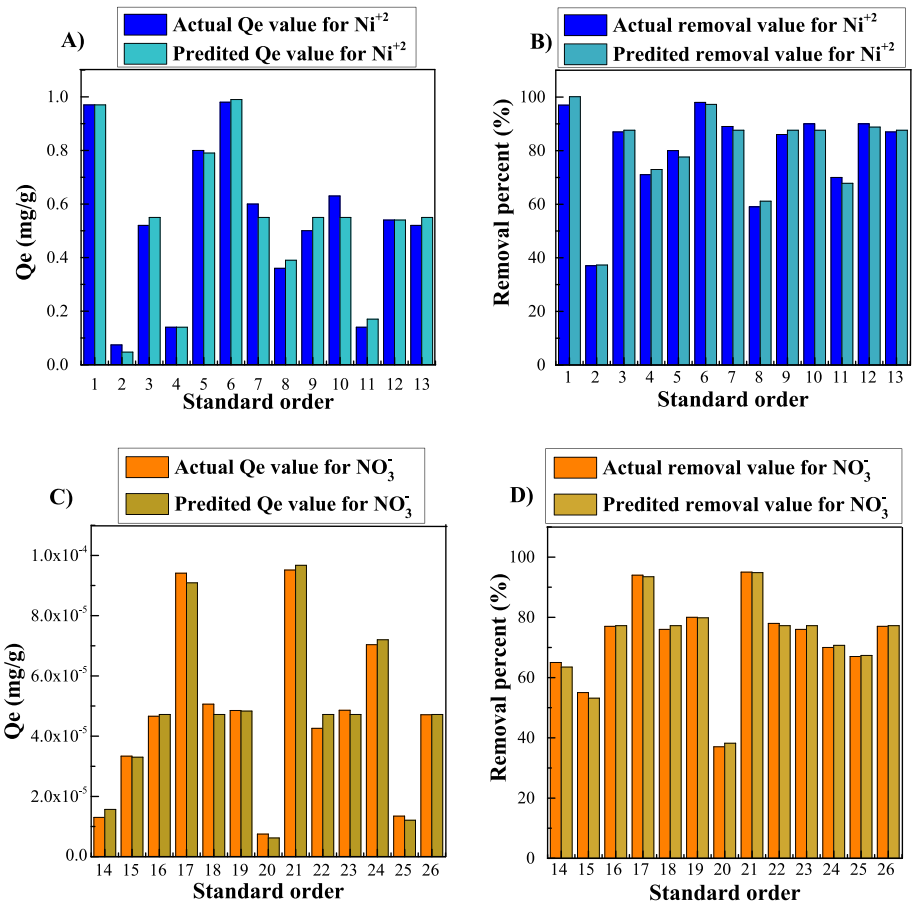

Fig. 10. The comparison of the empirical/ actual and predicted Qe (a and c) and removal percent (b and d) response values for Ni^{+2} (a and b) and NO_3^- (c and d) species.

assumption of constant variance. This plot should be a random distribution within the constant limitation of residuals across the graph. This random scattering is observed in Figs S12-S17 (b1 and b2) for both responses of all three nanocomposites. The predicted versus actual plot helps distinguish a value, or assembly of values, that are not easily predicted by the model. The data in this plot should be split through the 45-degree line. The presence of data close to 45-degree line in Figs S12-S17 (c1 and c2) indicates a good correlation between the experimental and predicted results (achieved by developed models) for both responses and whole nanocomposites ($R^2 > 0.96$).

As can be understood, the developed models passed the ANOVA standards well and can be applied to the detection of the most effective variables.

With regard to ANOVA analysis, and in order to compare the effectiveness of variables better, the percentage contribution of each term in the final developed models (according to estimation coefficients) for different responses are illustrated in Figs. 8 and 9. As revealed in Figs. 8 and 9, among the individual terms, the variable of species concentration (Ni^{+2} and NO_3^-) (A) are the most effective parameters on both Qe and removal responses. According to Figs. 8 and 9, for all nanocomposites upon Qe and removal percent responses, the interaction and squared terms have different contributions.

In fact, up to this step, using modeling of comprehensive experimental data and evaluation of estimation coefficients of different terms in developed models, it was revealed that the most effective variables on Qe and Removal percent responses for all three studied nanocomposites are species (Ni^{+2} or NO_3^-) concentration (A). In the next step, with regard to the detection of impressive variables using obtained results in the previous step, the central composite design (CCD) was done by considering three independent variables of weight percent of γ-Fe_2O_3, Ni^{+2} and NO_3^- concentration and the experimental design.

3.2.2. *The experimental design Approach: Part II: Response surface methodology combined with central composite design (CCD)*

Without expending a complete full factorial design of experiments, a face-centered central composite design matrix led to 13 experimental conditions (for each species (Ni^{+2} or NO_3^-)) established to create polynomials with quadratic terms. It is worth mentioning that because of different ranges of removed species concentrations (Ni^{+2} or NO_3^-), the designed experiments were illustrated in two tables. In CCD, each numeric variable is changed over 5 levels: plus, and minus one (factorial points), plus and minus alpha (axial points), and the center point. If categorical variables are added, the central composite design will be doubled for every combination of the categorical variable levels. Among 26 experiments designed, there are 5 center point runs for assessing pure error (for each species) due to random variation in the observed response. The considered independent variables in this part consist of weight percent of Fe_2O_3 in MoS_2/γ-Fe_2O_3 nanocomposites, Ni^{+2} concentration, and NO_3^- concentration, and selected responses are Qe and removal percent. It is worth mentioning that the reaction temperature and weight of nanocomposites were considered constant and at 50 °C and 0.005 g, respectively. The design summary, 26 runs performed, and related laboratory responses are provided in Tables 4 and 5.

With regard to the "sequential model sum of square" table provided by the software, the quadratic models with p-values < 0.0001 have been suggested as the most appropriate models for the Qe and removal percent responses. The statistical modeling of results was done separately for each species, and the final quadratic equations in terms of

actual variables for sufficiently forecasting Qe and removal percent were created as follows (Equations (15)-(18)):

For Ni^{+2}

$$Q_e = -0.38288 + (0.035569 \times Fe_2O_3) + (1.35549 \times (Conc. \times 10^{-4})) + (0.013496 \times Fe_2O_3 \times (Conc. \times 10^{-4})) - (8.09995E-004 \times Fe_2O_3^2) + (0.61994 \times (Conc. \times 10^{-4})^2) \quad (15)$$

$$Removal = -35.24856 + (7.05230 \times Fe_2O_3) + (175.91954 \times (Conc. \times 10^{-4})) - (2.0000 \times Fe_2O_3 \times (Conc. \times 10^{-4})) - (0.12672 \times Fe_2O_3^2) - (91.81034 \times (Conc. \times 10^{-4})^2) \quad (16)$$

For NO_3^-

$$Q_e = -2.29453E-005 + (2.67826E-006 \times Fe_2O_3) + (4.99529E-005 \times (Conc. \times 10^{-4})) + (2.35203E-006 \times Fe_2O_3 \times (Conc. \times 10^{-4})) - (6.54419E-008 \times Fe_2O_3^2) + (1.51780E-004 \times (Conc. \times 10^{-4})^2) \quad (17)$$

$$Removal = -15.73563 + (5.81049 \times Fe_2O_3) + (68.36207 \times (Conc. \times 10^{-4})) - (0.62500 \times Fe_2O_3 \times (Conc. \times 10^{-4})) - (0.10724 \times Fe_2O_3^2) + (31.89655 \times (Conc. \times 10^{-4})^2) \quad (18)$$

The statistical significance of models, the influence of individual and interaction of variables are confirmed by analysis of variance (Tables S17-S20).

As can be seen from Tables S17-S20, the obtained models passed the ANOVA standards well, and these developed models can be used to navigate the design space. The critical criteria that are well passed by the attained equations are summarized below (more detailed explanations about the interpretation of statistical parameters are given for Table 3 in the previous step): the high model F-value for Qe and removal percent responses and Ni^{+2} and NO_3^- species imply that the models are significant, values of "Prob > F" less than 0.0500 (<0.0001) indicate that the models terms are significant, the high amount of R^2 (>0.98), the "Pred $R^{2\prime\prime}$ are in reasonable agreement with the "Adj $R^{2\prime\prime}$ (the difference between these two parameters is less than 0.2), adequate precision of responses is desirable (greater than 4) and indicates an adequate signal, the non-significance of the lack of fit in whole responses (this parameter is an undesirable characteristic for a model, and then insignificant lack of fit is good).

The statistical validation of developed models could be graphically confirmed using the diagnostics plots, too. The obtained observations from different diagnostics graphs of both responses are as below (more detailed descriptions about the interpretation of diagnostic plots are given for Figs. S12-S17 in the previous step): a normal scattering of residuals closes a straight line in the "normal probability plot of residuals" (Fig. S18, a1-a4), a random distribution within the constant limitation of residuals across the "residuals versus predicted graph" (Fig. S18, b1-b4), good correlation between the experimental and predicted results in "predicted versus actual plots" (Fig. S18 c1-c4).

The good fitting potency of developed models is confirmed by comparison of empirical and predicted response values, as shown in Fig. 10.

In the following, in order to gain graphical insight into the binary effect of two independent variables of the weight percent of γ-Fe_2O_3 (A) and species concentration (B) on the Qe and removal percent responses, for each species of Ni^{+2} and NO_3^-, 3D and 2D (contour) plots were investigated. In the case of the binary influence of weight percent of γ-Fe_2O_3 (A) and species concentration (B) on the Qe response of Ni^{+2} species (Fig. 11a), it was revealed that an increase in both A and B parameters leads to an increase in Qe response, but this increase is steeper for B rather than variations. A maximum in Qe was found at a weight percent of γ-Fe_2O_3 of around 30 % and Ni^{+2} concentration of 0.5×10^{-4} mol.L^{-1}. As revealed from Fig. 11a, both parameters had a positive effect on Qe, but parameter B (species concentration) was the most significant. These evidences are in good agreement with the consequences of the ANOVA study.

The binary effect of weight percent of γ-Fe_2O_3 (A) and species concentration (B) on the removal percent response of Ni^{+2} species is shown in Fig. 11b. As shown, a sharp increase in removal percent was observed with an increase in Ni^{+2} concentration at a low weight percent of γ-Fe_2O_3 and an increase in weight percent of γ-Fe_2O_3 at low Ni^{+2} concentration, while a soft increase in removal percent was detected at high Ni^{+2} concentration and weight percent of γ-Fe_2O_3. It can be seen that the effect of one parameter (A or B) on the considered response depended on the other one (B or A). This behavior points to the binary effect between parameters (A and B). According to Fig. 11b, minimum removal percent was associated with low weight percent of γ-Fe_2O_3 and Ni^{+2} concentration.

Similar results were found from Qe and removal percent plot for NO_3^- species.

Using the output functions of the DoE (Eqs. 15–18) to establish the relationships between variables and responses, the multiple-objective optimization of the process was investigated. One of the solutions for maximizing Qe and removal percent for Ni^{+2} species with a desirability value of one was 26.72 % for weight percent of γ-Fe_2O_3 and Ni^{+2} concentration of 0.49 mol.L^{-1} with a predicted Qe and removal percent of 0.98 mg/g and 100 %, respectively. One of the predicted values for maximizing Qe and removal percent for NO_3^- species with a desirability value of one was 27.55 % for weight percent of γ-Fe_2O_3 and NO_3^- concentration of 0.50×10^{-4} mol.L^{-1} with a predicted Qe and removal percent of 9.59×10^{-5} mg/g and 96.33 %, respectively. To validate the optimized result, a fresh nanocomposite with recommended conditions was fabricated in the lab. The empirical and software predicted results demonstrated a good correlation (Table 6).

4. Conclusion

In this work, superparamagnetic MoS_2/γ-Fe_2O_3 (10, 20, and 30 %) nanocomposites (with the morphology of like-flower) were prepared by loading various percentages of γ-Fe_2O_3 (10, 20, and 30 %) nanoparticles on surface MoS_2. Nanocomposites are reported as efficient adsorptions for removal of Ni^{+2} and NO_3^- ions from aqueous media that were studied by using the experimental design in two steps. In the first step, the modeling of the effect of independent synthesis conditions including the concentration of Ni^{+2} and NO_3^-, the weight of the catalyst, and reaction temperature, for the adsorption capacities and removal percent of the three superparamagnetic nanocomposites were performed using response surface methodology (RSM); and the most effective variables were recognized (species concentrations). In the following, the central composite design and optimization of synthesis parameters were performed using the most important variables recognized. The maximum

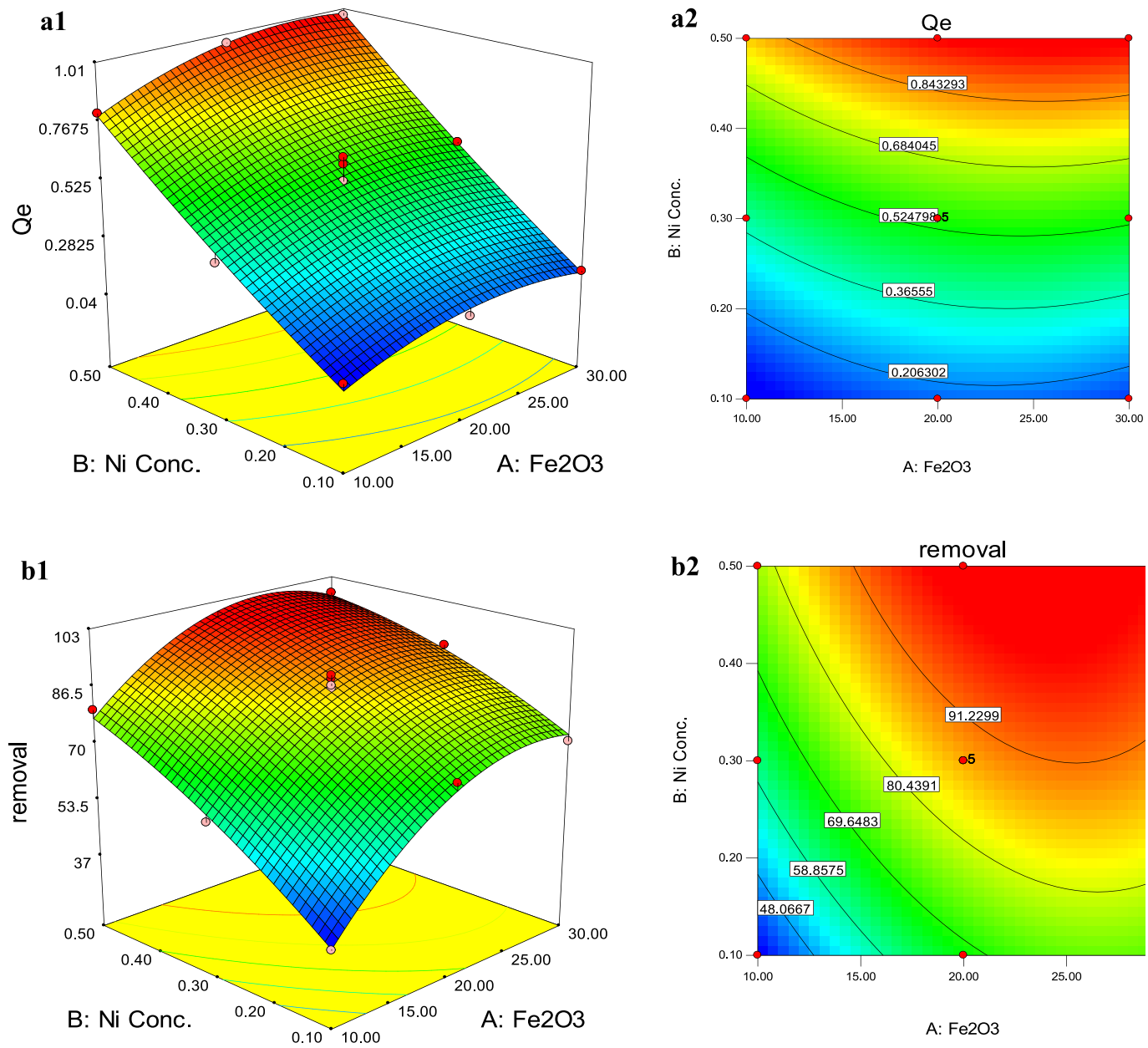

Fig. 11. 3D and contour plots for Qe (a1-2 and c1-2) and removal percent (b1-2 and d1-2) of Ni^{+2} (a and b) and NO_3^- (c and d) species.

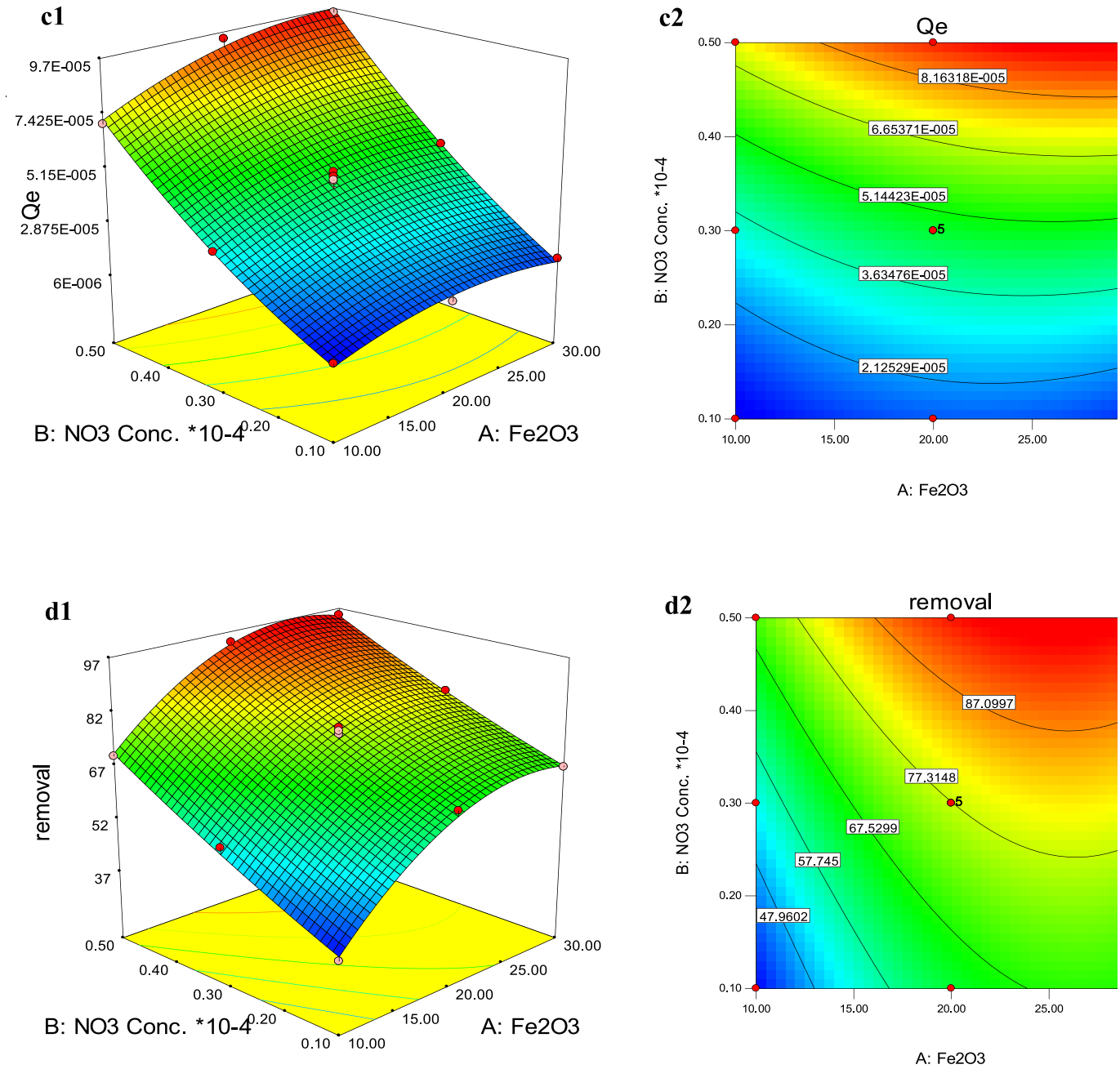

Fig. 11. (*continued*).

Table 6
Comparison of predicted and obtained results for DoE optimized nanocomposite.

Species	Ni^{+2}	NO_3^-
Species concentration (mol.L^{-1})	0.49	0.50×10^{-4}
Weight percent of γ-Fe_2O_3 (%)	26.72	27.55
Predicted Qe (mg/g)	0.98	9.59×10^{-5}
Experimental Qe (mg/g)	0.95	9.23×10^{-5}
Predicted removal percent (%)	100	96.33
Experimental removal percent (%)	96	93

adsorption capacities and removal percent of the MoS_2/γ-Fe_2O_3 nanocomposites were forecast and empirically approved which proved a suitable agreement. The optimized conditions for Ni^{+2} species are Ni^{+2} concentration = 0.49 mol.L^{-1}, and weight percent of γ-Fe_2O_3 = 26.72 % with predicted Qe = 0.98 mg/g and removal percent = 100 %, and for NO^{-3} species are NO^{-3} concentration = 0.50×10^{-4} mol.L^{-1} and weight percent of γ-Fe_2O_3 = 27.55 % with predicted Qe = 9.59×10^{-5} mg/g and removal percent = 96.33 %. The results obtained from Ni^{2+} and NO^{-3} ions indicate the experimental Qe of 0.95 and 9.23×10^{-5} (mg/g), and the removal percentage of 96 and 93(%), the presence 26.72 and 27.55 (%) dose of MoS_2/γ-Fe_2O_3 nanocomposites. Experimental investigations showed that the application of nanocomposites with recyclability is favorable to water treatment and the retention of the environment from wastewater pollution. The modeling study with the purpose of assessment of the prominence of individual/binary impacts of synthesis variables on responses, ANOVA, and optimization were successfully performed by response surface and design expert 7.0.0 software. Regarding the using of the RSM method, it should be mentioned that by using the usual experimental method we can see the influence of each selected parameter lonely on the catalyst performance while all of the other factors were kept constant. However, RSM method enables us to observe the influence of all of these selected parameters concurrently

upon the catalyst performance.

CRediT authorship contribution statement

Somayeh Ostovar: Conceptualization, Methodology, Formal analysis, Data curation, Writing – original draft. **Hamideh Saravani:** Supervision. **Maryam Akbari:** Formal analysis. **Amanolah Salehpour:** Investigation. **Mohammad Sabaghi:** Investigation. **Esmaiel Rezazadeh:** .

Declaration of Competing Interest

The authors declare that they have no known competing financial interests or personal relationships that could have appeared to influence the work reported in this paper.

Acknowledgment:

H. Saravani gratefully acknowledges the financial support of the research Iran National Science Foundation (Grant No. 98004213) as well, complementary financial supports of Sistan and Balouchestan University of Iran.

Appendix A. Supplementary material

Supplementary data to this article can be found online at https://doi.org/10.1016/j.arabjc.2024.105599.

References

Abascal, E., Gómez-Coma, L., Ortiz, I., Ortiz, A., 2022. Global diagnosis of nitrate pollution in groundwater and review of removal technologies. Sci. Total Environ. 810, 152233.
Abujazar, M.S.S., Karaağaç, S.U., Amr, S.S.A., Alazaiza, M.Y., Bashir, M.J., 2022. Recent advancement in the application of hybrid coagulants in coagulation-flocculation of wastewater: A review. J. Clean. Prod. 131133.
Aghagoli, M.J., Beyki, M.H., Shemirani, F., 2017. Application of dahlia-like molybdenum disulfide nanosheets for solid phase extraction of Co (II) in vegetable and water samples. Food Chem. 223, 8–15.
Aghagoli, M.J., Shemirani, F., 2017. Hybrid nanosheets composed of molybdenum disulfide and reduced graphene oxide for enhanced solid phase extraction of Pb (II) and Ni (II). Mikrochim. Acta 184 (1), 237–244.
Akbari, M., Mirzaei, A.A., Atashi, H., 2019. Evaluation of reverse microemulsion parameters over the catalytic performance of promoted Fe–Co catalysts for the production of light olefins from syngas using box–behnken design. Catal Lett 149 (5), 1305–1318.
Ali, N., Riead, M.M.H., Bilal, M., Yang, Y., Khan, A., Ali, F., Sher, F., 2021. Adsorptive remediation of environmental pollutants using magnetic hybrid materials as platform adsorbents. Chemosphere 284, 131279.
Al-Maliky, E.A., Gzar, H.A., Al-Azawy, M.G., 2021. Determination of point of zero charge (PZC) of concrete particles adsorbents. Paper Presented at the IOP Conference Series: Materials Science and Engineering.
Alqadami, A.A., Naushad, M., Abdalla, M.A., Ahamad, T., AlOthman, Z.A., Alshehri, S. M., Ghfar, A.A., 2017. Efficient removal of toxic metal ions from wastewater using a recyclable nanocomposite: a study of adsorption parameters and interaction mechanism. J. Clean. Prod. 156, 426–436.
Alsubih, M., El Morabet, R., Khan, R.A., Khan, N.A., Khan, A.R., Khan, S., Yousefi, M., 2022. Performance evaluation of constructed wetland for removal of pharmaceutical compounds from hospital wastewater: Seasonal perspective. Arab. J. Chem. 15 (12), 104344.
Amanollahi, H., Moussavi, G., Ostovar, S., Giannakis, S., 2023. From waste to wealth: Using MgO nanoparticles to transform ammonium into a valuable resource. J. Water Process Eng. 56, 104331.
Anderson, A., Anbarasu, A., Pasupuleti, R.R., Sekar, M., Praveenkumar, T., Kumar, J.A., 2022. Treatment of heavy metals containing wastewater using biodegradable adsorbents: A review of mechanism and future trends. Chemosphere 133724.
Bagheri, F., Chaibakhsh, N., 2020. Efficient visible-light photocatalytic ozonation for dye degradation using Fe_2O_3/MoS_2 nanocomposite. Sep Sci Technol 1–11.
Bahrami, M., Amiri, M.J., 2022. Nitrate removal from contaminated waters using modified rice husk ash by Hexadecyltrimethylammonium bromide surfactant. React. Kinet. Mech. Catal. 135 (1), 459–478.
Bardestani, R., Patience, G.S., Kaliaguine, S., 2019. Experimental methods in chemical engineering: specific surface area and pore size distribution measurements—BET, BJH, and DFT. Can J Chem Eng. 97 (11), 2781–2791.
Barua, S., Dutta, H.S., Gogoi, S., Devi, R., Khan, R., 2017. Nanostructured MoS_2-based advanced biosensors: a review. ACS Appl. Nano Mater. 1 (1), 2–25.
Benalia, M.C., Youcef, L., Bouaziz, M.G., Achour, S., Menasra, H., 2022. Removal of heavy metals from industrial wastewater by chemical precipitation: mechanisms and sludge characterization. Arab J Sci Eng 47 (5), 5587–5599.
Benhammou, A., Yaacoubi, A., Nibou, L., Tanouti, B., 2005. Adsorption of metal ions onto Moroccan stevensite: kinetic and isotherm studies. J. Colloid Interface Sci. 282 (2), 320–326.
Bethi, B., Sonawane, S.H., Bhanvase, B.A., Gumfekar, S.P., 2016. Nanomaterials-based advanced oxidation processes for wastewater treatment: A review. Chem. Eng. Process.: Process Intensif. 109, 178–189.
Bolisetty, S., Peydayesh, M., Mezzenga, R., 2019. Sustainable technologies for water purification from heavy metals: review and analysis. Chem. Soc. Rev. 48 (2), 463–487.
Boulaiche, W., Hamdi, B., Trari, M., 2019. Removal of heavy metals by chitin: equilibrium, kinetic and thermodynamic studies. Appl. Water Sci. 9, 1–10.
Brusseau, M.L., Artiola, J., 2019. Chemical contaminants. In: Environmental and Pollution Science. Elsevier, pp. 175–190.
Buruga, K., Song, H., Shang, J., Bolan, N., Jagannathan, T.K., Kim, K.-H., 2019. A review on functional polymer-clay based nanocomposite membranes for treatment of water. J. Hazard. Mater. 379, 120584.
Chakraborty, R., Asthana, A., Singh, A.K., Jain, B., Susan, A.B.H., 2022. Adsorption of heavy metal ions by various low-cost adsorbents: a review. Int J Environ Anal Chem. 102 (2), 342–379.
Choi, W.S., Lee, H.-J., 2022. Nanostructured materials for water purification: Adsorption of heavy metal ions and organic dyes. Polymers 14 (11), 2183.
Choudhary, M., Peter, C., Shukla, S.K., Govender, P.P., Joshi, G.M., Wang, R., 2020. Environmental issues: a challenge for wastewater treatment. Green Mater. 1–12.
Fei, Y., Hu, Y.H., 2022. Design, synthesis, and performance of adsorbents for heavy metal removal from wastewater: a review. J. Mater. Chem. 10 (3), 1047–1085.
Gabrielsson, J., Lindberg, N.O., Lundstedt, T., 2002. Multivariate methods in pharmaceutical applications. J. Chemom. 16 (3), 141–160.
Gao, Y., Chen, C., Tan, X., Xu, H., Zhu, K., 2016. Polyaniline-modified 3D-flower-like molybdenum disulfide composite for efficient adsorption/photocatalytic reduction of Cr (VI). J. Colloid Interface Sci. 476, 62–70.
Ghomi Avili, F., 2021. Removal of heavy metals (lead and nickel) from water sources by adsorption of activated alumina. Anthropog. Pollut 5 (2), 1–7.
Goswami, R.K., Mehariya, S., Karthikeyan, O.P., Gupta, V.K., Verma, P., 2022. Multifaceted application of microalgal biomass integrated with carbon dioxide reduction and wastewater remediation: A flexible concept for sustainable environment. J. Clean. Prod. 339, 130654.
GUILHEN, S. N., Watanabe, T., SILVA, T. T., Rovani, S., MARUMO, J. T., TENORIO, J. A., . . . ARAUJO, L. G. d. 2022. Role of point of zero charge in the adsorption of cationic textile dye on standard biochars from aqueous solutions. Recent prog. mater.
Günay, A., Arslankaya, E., Tosun, I., 2007. Lead removal from aqueous solution by natural and pretreated clinoptilolite: adsorption equilibrium and kinetics. J. Hazard. Mater. 146 (1–2), 362–371.
Gusain, R., Kumar, N., Ray, S.S., 2020. Recent advances in carbon nanomaterial-based adsorbents for water purification. Coord Chem Rev. 405, 213111.
Han, C., Huang, G., Zhu, D., Hu, K., 2017. Facile synthesis of MoS_2/Fe_3O_4 nanocomposite with excellent Photo-Fenton-like catalytic performance. Mater. Chem. Phys. 200, 16–22.
Hao, L., Zhou, X., Liu, J., 2020. Release of ZrO_2 nanoparticles from ZrO_2/Polymer nanocomposite in wastewater treatment processes. J. Environ. Sci. 91, 85–91.
Haque, S.M., Rahman, H., Rahman, N., Azmi, S.N.H., Ashwaq, O., Wabaidur, S.M., Alam, M., 2023. Application of Box-Behnken design combined response surface methodology to optimize HPLC and spectrophotometric techniques for quantifying febuxostat in pharmaceutical formulations and spiked wastewater samples. Microchem. J. 184, 108191.
Harja, M., Ciobanu, G., 2020. Eco-friendly Nano-adsorbents for Pollutant Removal from Wastewaters. Handbook of Nanomaterials and Nanocomposites for Energy and Environmental Applications 1–22.
He, P., Zhao, X., Luo, F., Zhang, Y., Wei, J., Xu, T., Chen, N., 2020. Magnetically recyclable Fe_3O_4 doped flower-like MoS_2: Efficient removal of elemental mercury. Fuel 282, 118728.
Hmoud Al-Adhaileh, M., Waselallah Alsaade, F., 2021. Modelling and prediction of water quality by using artificial intelligence. Sustainability 13 (8), 4259.
Hoang, A.T., Nižetić, S., Cheng, C.K., Luque, R., Thomas, S., Banh, T.L., Nguyen, X.P., 2022. Heavy metal removal by biomass-derived carbon nanotubes as a greener environmental remediation: A comprehensive review. Chemosphere 287, 131959.
Hu, S., Chen, W., Zhou, J., Yin, F., Uchaker, E., Zhang, Q., Cao, G., 2014. Preparation of carbon coated MoS_2 flower-like nanostructure with self-assembled nanosheets as high-performance lithium-ion battery anodes. J. Mater. Chem. 2 (21), 7862–7872.
Huang, Y., Zeng, X., Guo, L., Lan, J., Zhang, L., Cao, D., 2018. Heavy metal ion removal of wastewater by zeolite-imidazolate frameworks. Sep. Purif. Technol. 194, 462–469.
Ighalo, J.O., Adeniyi, A.G., 2020. A comprehensive review of water quality monitoring and assessment in Nigeria. Chemosphere 260, 127569.
Janani, R., Gurunathan, B., Sivakumar, K., Varjani, S., Ngo, H.H., Gnansounou, E., 2022. Advancements in heavy metals removal from effluents employing nano-adsorbents: way towards cleaner production. Environ. Res. 203, 111815.
Jun, B.-M., Lee, H.-K., Park, S., Kim, T.-J., 2021. Purification of uranium-contaminated radioactive water by adsorption: A review on adsorbent materials. Sep. Purif. Technol. 278, 119675.
Karimifard, S., Moghaddam, M.R.A., 2018. Application of response surface methodology in physicochemical removal of dyes from wastewater: a critical review. Sci. Total Environ. 640, 772–797.

Kesari, K.K., Soni, R., Jamal, Q.M.S., Tripathi, P., Lal, J.A., Jha, N.K., Ruokolainen, J., 2021. Wastewater treatment and reuse: a review of its applications and health implications. Water Air Soil Pollut 232, 1–28.
Kiani, B., Hashemi Amin, F., Bagheri, N., Bergquist, R., Mohammadi, A.A., Yousefi, M., Rahimzadeh, H., 2021. Association between heavy metals and colon cancer: an ecological study based on geographical information systems in North-Eastern Iran. BMC Cancer 21 (1), 1–12.
Kong, Y., Wang, L., Ge, Y., Su, H., Li, Z., 2019. Lignin xanthate resin–bentonite clay composite as a highly effective and low-cost adsorbent for the removal of doxycycline hydrochloride antibiotic and mercury ions in water. J. Hazard. Mater. 368, 33–41.
Kothavale, V., Sharma, A., Dhavale, R., Chavan, V., Shingte, S., Selyshchev, O., Salvan, G., 2022. Hyperbranched amino modified magnetic nanoparticles for simultaneous removal of heavy metal ions from aqueous solutions. Mater. Chem. Phys. 292, 126792.
Krishna Kumar, A.S., Jiang, S.-J., Warchoł, J.K., 2017. Synthesis and characterization of two-dimensional transition metal dichalcogenide magnetic MoS_2@Fe_3O_4 nanoparticles for adsorption of Cr(VI)/Cr(III). ACS Omega 2 (9), 6187–6200.
Kumar, N., Reddy, L., Parashar, V., Ngila, J.C., 2017. Controlled synthesis of microsheets of ZnAl layered double hydroxides hexagonal nanoplates for efficient removal of Cr (VI) ions and anionic dye from water. J. Environ. Chem. Eng. 5 (2), 1718–1731.
Lahnafi, A., Elgamouz, A., Tijani, N., Jaber, L., Kawde, A.-N., 2022. Hydrothermal synthesis and electrochemical characterization of novel zeolite membranes supported on flat porous clay-based microfiltration system and its application of heavy metals removal of synthetic wastewaters. Microporous Mesoporous Mater. 334, 111778.
Lande, M., Phatake, V., Chavha, P., Chaudhari, M., Raundal, S., Salunke, H., 2020. Role of nanotechnology to control water pollution. Int. J. RES, Biosci.
Li, X.L., Li, T.C., Huang, S., Zhang, J., Pam, M.E., Yang, H.Y., 2020. Controllable Synthesis of Two-Dimensional Molybdenum Disulfide (MoS_2) for Energy-Storage Applications. ChemSusChem.
Li, J., Tang, W., Yang, H., Dong, Z., Huang, J., Li, S., Ma, J., 2014. Enhanced-electrocatalytic activity of Ni 1–x Fe x alloy supported on polyethyleneimine functionalized MoS_2 nanosheets for hydrazine oxidation. RSC Adv. 4 (4), 1988–1995.
Li, C., Zhang, S., Zhou, Y., Li, J., 2017. A situ hydrothermal synthesis of a two-dimensional MoS_2/TiO_2 heterostructure composite with exposed (001) facets and its visible-light photocatalytic activity. J. Mater. Sci. 28 (12), 9003–9010.
Lin, X., Wang, X., Zhou, Q., Wen, C., Su, S., Xiang, J., Wang, X., 2018. Magnetically recyclable MoS_2/Fe_3O_4 hybrid composite as visible light responsive photocatalyst with enhanced photocatalytic performance. ACS Sustain. Chem. Eng. 7 (1), 1673–1682.
Liu, J., Du, J., Su, Y., Zhao, H., 2019. A facile solvothermal synthesis of 3D magnetic MoS_2/Fe_3O_4 nanocomposites with enhanced peroxidase-mimicking activity and colorimetric detection of perfluorooctane sulfonate. Microchem. J. 149, 104019.
Liu, C., Jia, F., Wang, Q., Yang, B., Song, S., 2017. Two-dimensional molybdenum disulfide as adsorbent for high-efficient Pb(II) removal from water. Appl. Mater. Today 9, 220–228.
Liu, Q., Li, X., He, Q., Khalil, A., Liu, D., Xiang, T., Song, L., 2015. Gram-scale aqueous synthesis of stable few-layered 1T-MoS2: applications for visible-light-driven photocatalytic hydrogen evolution. Small 11 (41), 5556–5564.
Liu, X., Li, Y., Chen, Z., Yang, H., Cai, Y., Wang, S., Shen, C., 2023. Advanced porous nanomaterials as superior adsorbents for environmental pollutants removal from aqueous solutions. Crit Rev Environ Sci Technol 1–21.
Lu, S., Ma, Y., Zhao, L., 2022. Production of ZnO-CoO_x-CeO_2 nanocomposites and their dye removal performance from wastewater by adsorption-photocatalysis. J. Mol. Liq. 364, 119924.
Ma, W., Row, K.H., 2020. Solid-phase extraction of catechins from green tea with deep eutectic solvent immobilized magnetic molybdenum disulfide molecularly imprinted polymer. Molecules 25 (2), 280.
Ma, L., Wang, Q., Islam, S.M., Liu, Y., Ma, S., Kanatzidis, M.G., 2016. Highly selective and efficient removal of heavy metals by layered double hydroxide intercalated with the MoS_{42}–ion. J. Am. Chem. Soc. 138 (8), 2858–2866.
Ma, J., Zhou, G., Chu, L., Liu, Y., Liu, C., Luo, S., Wei, Y., 2017. Efficient removal of heavy metal ions with an EDTA functionalized chitosan/polyacrylamide double network hydrogel. ACS Sustain. Chem. Eng. 5 (1), 843–851.
Madima, N., Mishra, S., Inamuddin, I., Mishra, A., 2020. Carbon-based nanomaterials for remediation of organic and inorganic pollutants from wastewater. A Review. Environ. Chem. Lett. 18, 1169–1191.
Maharana, M., Manna, M., Sardar, M., Sen, S., 2021. Heavy metal removal by low-cost adsorbents. Green Adsorbents to Remove Metals, Dyes and Boron from Polluted Water, pp. 245–272.
Mahmoudian, M.H., Azari, A., Jahantigh, A., Sarkhosh, M., Yousefi, M., Razavinasab, S. A., Zeidabadi, A., 2023. Statistical modeling and optimization of dexamethasone adsorption from aqueous solution by Fe_3O_4@ NH_2-MIL88B nanorods: Isotherm, kinetics, and thermodynamic. Environ. Res. 236, 116773.
Manos, M.J., Kanatzidis, M.G., 2016. Metal sulfide ion exchangers: superior sorbents for the capture of toxic and nuclear waste-related metal ions. Chem. Sci. 7 (8), 4804–4824.
Mariana, M., HPS, A. K., Mistar, E., Yahya, E. B., Alfatah, T., Danish, M., and Amayreh, M. 2021. Recent advances in activated carbon modification techniques for enhanced heavy metal adsorption. J. Water Process Eng., 43, 102221.
Mirzaei, A.A., Farahi, M., Akbari, M., 2021. Effect of reduction and reaction conditions on the catalytic performance of Co–Ni/Al_2O_3 catalyst in CO hydrogenation: modeling of surface reaction rate. CHEM PAP 75 (5), 2087–2103.
Mu, D., Chen, Z., Shi, H., Tan, N., 2018. Construction of flower-like MoS_2/Fe_3O_4/rGO composite with enhanced photo-Fenton like catalyst performance. RSC Adv. 8 (64), 36625–36631.
Najmaei, S., Zou, X., Er, D., Li, J., Jin, Z., Gao, W., Lei, S., 2014. Tailoring the physical properties of molybdenum disulfide monolayers by control of interfacial chemistry. Nano Lett. 14 (3), 1354–1361.
Nayak, S., Harms, K., Dehnen, S., 2011. New Three-Dimensional Metal− Organic Framework with Heterometallic [Fe−Ag] Building Units: Synthesis, Crystal Structure, and Functional Studies. Inorg. Chem. 50 (7), 2714–2716.
Niu, Y., Qu, R., Sun, C., Wang, C., Chen, H., Ji, C., Bu, F., 2013. Adsorption of Pb(II) from aqueous solution by silica-gel supported hyperbranched polyamidoamine dendrimers. J. Hazard. Mater. 244, 276–286.
Numan, A., Gill, A.A., Rafique, S., Guduri, M., Zhan, Y., Maddiboyina, B., Dang, N.N., 2021. Rationally engineered nanosensors: A novel strategy for the detection of heavy metal ions in the environment. J. Hazard. Mater. 409, 124493.
Ostovar, S., Rodríguez-Padrón, D., Saberi, F., Balu, A.M., Luque, R., 2019. Versatile sulfathiazole-functionalized magnetic nanoparticles as catalyst in oxidation and alkylation reactions. Catalysts 9 (4), 348.
Ostovar, S., Moussavi, G., Mohammadi, S., Marin, M.L., Bosca, F., Diego-Lopez, A., Giannakis, S., 2023a. Developing a novel Ti-doped ɣAl2O3 xerogel with high photocatalytic chemical and microbial removal performance: Characterization and mechanistic insights. Chem. Eng. Technol. 464, 142545.
Ostovar, S., Moussavi, G., Mohammadi, S., Marin, M.L., Bosca, F., Diego-Lopez, A., Giannakis, S., 2023b. Rapid degradation of Omeprazole and highly effective inactivation of E. coli in the UVA-light photocatalytic process with Cu-doped in spinel-structured ɣAl2O3 as a stable catalyst. Chem. Eng. Technol. 147536.
Pincus, L.N., Lounsbury, A.W., Zimmerman, J.B., 2019. Toward realizing multifunctionality: Photoactive and selective adsorbents for the removal of inorganics in water treatment. Acc. Chem. Res. 52 (5), 1206–1214.
Priyadarshanee, M., Das, S., 2021. Biosorption and removal of toxic heavy metals by metal tolerating bacteria for bioremediation of metal contamination: A comprehensive review. J. Environ. Chem. Eng. 9 (1), 104686.
Pronk, W., Ding, A., Morgenroth, E., Derlon, N., Desmond, P., Burkhardt, M., Fane, A.G., 2019. Gravity-driven membrane filtration for water and wastewater treatment: a review. Water Res. 149, 553–565.
Rad, L.R., Anbia, M., 2021. Zeolite-based composites for the adsorption of toxic matters from water: A review. J. Environ. Chem. Eng. 9 (5), 106088.
Rahman, N., Khan, M.F., 2016. Nitrate removal using poly-o-toluidine zirconium (IV) ethylenediamine as adsorbent: Batch and fixed-bed column adsorption modelling. J. Water Process Eng. 9, 254–266.
Rahman, N., Nasir, M., Bharti, M., Samdani, M.S., 2023a. Fabrication of Zero-Valent Iron Nanoparticles Impregnated Cross-Linked Chitosan Grafted β-Cyclodextrin for Removal of Cloxacillin from Aqueous Environment. J. Inorg. Organomet. Polym. Mater. 1–24.
Rahman, N., Raheem, A., 2023b. Mechanistic investigation of levofloxacin adsorption on Fe (III)-tartaric acid/xanthan gum/graphene oxide/polyacrylamide hydrogel: Box-Behnken design and Taguchi method for optimization. J. Ind. Eng. Chem. 127, 110–124.
Rahman, N., Raheem, A., Nasir, M., Franco, D.S., 2023b. Fractal-like kinetic modelling for sorption of diclofenac onto graphene oxide/polypyrrole composite: Mechanism analysis and response surface methodology for optimization. Diam. Relat. Mater. 139, 110328.
Rahman, N., Varshney, P., 2020. Assessment of ampicillin removal efficiency from aqueous solution by polydopamine/zirconium (iv) iodate: optimization by response surface methodology. RSC Adv. 10 (34), 20322–20337.
Ren, X., Chen, C., Nagatsu, M., Wang, X., 2011. Carbon nanotubes as adsorbents in environmental pollution management: a review. Chem. Eng. Technol. 170 (2–3), 395–410.
Saberi, F., Ostovar, S., Behazin, R., Rezvani, A., Ebrahimi, A., Shaterian, H.R., 2020. Insight into 6-aminopenicillanic acid structure and study of the quantum mechanical calculations of the acid–base site on γ-Fe_2O_3@SiO_2 core–shell nanocomposites and as efficient catalysts in multicomponent reactions. New J Chem 44 (47), 20688–20696.
Saleh, T.A., Mustaqeem, M., Khaled, M., 2022. Water treatment technologies in removing heavy metal ions from wastewater: A review. Environ. Nanotechnol. Monit. Manag. 17, 100617.
Sedighi, M., Usefi, M.M.B., Ismail, A.F., Ghasemi, M., 2023. Environmental sustainability and ions removal through electrodialysis desalination: Operating conditions and process parameters. Desalination 549, 116319.
Setayesh, S.R., Nazari, P., Maghbool, R., 2020. Engineered $FeVO_4/CeO_2$ nanocomposite as a two-way superior electro-Fenton catalyst for model and real wastewater treatment. J. Environ. Sci. 97, 110–119.
Sheerazi, Z., Ahmed, M., 2022. Nano-Adsorbents and Nano-Catalysts for Wastewater Treatment. In: Emerging Nanomaterials for Advanced Technologies. Springer, pp. 517–539.
Shen, Y., Chen, B., 2015. Sulfonated graphene nanosheets as a superb adsorbent for various environmental pollutants in water. Environ. Sci. Technol. 49 (12), 7364–7372.
Sheth, Y., Dharaskar, S., Khalid, M., Sonawane, S., 2021. An environment friendly approach for heavy metal removal from industrial wastewater using chitosan based biosorbent: A review. Sustain. Energy Technol. Assess. 43, 100951.
Singh, V.V., Kaufmann, K., de Ávila, B.E.F., Karshalev, E., Wang, J., 2016. Molybdenum Disulfide-Based Tubular Microengines: Toward Biomedical Applications. Adv. Funct. Mater. 26 (34), 6270–6278.
Singh, N., Nagpal, G., Agrawal, S., 2018. Water purification by using adsorbents: a review. Environ. Technol. Innov. 11, 187–240.

Singh, T.S., Pant, K., 2004. Equilibrium, kinetics and thermodynamic studies for adsorption of As (III) on activated alumina. Sep. Purif. Technol. 36 (2), 139–147.
Singh, S., Wasewar, K.L., Kansal, S.K., 2020. In: Low-Cost Adsorbents for Removal of Inorganic Impurities from Wastewater. Elsevier, pp. 173–203.
Sinha, P., Datar, A., Jeong, C., Deng, X., Chung, Y.G., Lin, L.-C., 2019. Surface area determination of porous materials using the Brunauer–Emmett–Teller (BET) method: limitations and improvements. J. Phys. Chem. C 123 (33), 20195–20209.
Song, Y., Lu, M., Huang, B., Wang, D., Wang, G., Zhou, L., 2018. Decoration of defective MoS_2 nanosheets with Fe_3O_4 nanoparticles as superior magnetic adsorbent for highly selective and efficient mercury ions (Hg^{2+}) removal. J. Alloys Compd. 737, 113–121.
Song, X., Ren, C., Zhao, Q., Su, B., 2020. Simultaneous removal of Cr(VI) and triclosan from aqueous solutions through Fe_3O_4 magnetic nanoscale-activated persulfate oxidation. Chem. Eng. Technol. 381, 122586.
Swanckaert, B., Geltmeyer, J., Rabaey, K., De Buysser, K., Bonin, L., De Clerck, K., 2022. A review on ion-exchange nanofiber membranes: properties, structure and application in electrochemical (waste) water treatment. Sep. Purif. Technol. 287, 120529.
Tanweer, M.S., Chauhan, H., Alam, M., 2022. Advanced 2D Nanomaterial Composites: Applications in Adsorption of Water Pollutants and Toxic Gases. In: 2D Nanomaterials for Energy and Environmental Sustainability. Springer, pp. 97–124.
Thangadurai, D., Ahuja, V., Sangeetha, J., 2020. Nanomaterials and Nanoprocesses for the Removal and Reuse of Heavy Metals. Handbook of Nanomaterials and Nanocomposites for Energy and Environmental Applications 1–12.
Torkashvand, J., Saeedi-Jurkuyeh, A., Rezaei Kalantary, R., Gholami, M., Esrafili, A., Yousefi, M., Farzadkia, M., 2022. Preparation of a cellulose acetate membrane using cigarette butt recycling and investigation of its efficiency in removing heavy metals from aqueous solution. Sci. Rep. 12 (1), 20336.
Vidu, R., Matei, E., Predescu, A.M., Alhalaili, B., Pantilimon, C., Tarcea, C., Predescu, C., 2020. Removal of heavy metals from wastewaters: A challenge from current treatment methods to nanotechnology applications. Toxics 8 (4), 101.
Vishwakarma, V., 2021. Recovery and recycle of wastewater contaminated with heavy metals using adsorbents incorporated from waste resources and nanomaterials-A review. Chemosphere 129677.
Wang, Y., Bao, S., Liu, Y., Yu, Y., Yang, W., Xu, S., Li, H., 2021. CoS_2/GO nanocomposites for highly efficient and ppb level adsorption of Hg (II) from wastewater. J. Mol. Liq. 322, 114899.
Wang, X., Cheng, H., Ye, G., Fan, J., Yao, F., Wang, Y., Ye, D., 2022. Key factors and primary modification methods of activated carbon and their application in adsorption of carbon-based gases: A review. Chemosphere 287, 131995.
Wang, Z., Mi, B., 2017. Environmental applications of 2D molybdenum disulfide (MoS_2) nanosheets. Environ. Sci. Technol. 51 (15), 8229–8244.
Wang, Z., Sim, A., Urban, J.J., Mi, B., 2018. Removal and recovery of heavy metal ions by two-dimensional MoS_2 nanosheets: performance and mechanisms. Environ. Sci. Technol. 52 (17), 9741–9748.
Wang, G., Wang, S., Sun, W., Sun, Z., Zheng, S., 2017a. Synthesis of a novel illite@ carbon nanocomposite adsorbent for removal of Cr (VI) from wastewater. J. Environ. Sci. 57, 62–71.
Wang, J., Wang, P., Wang, H., Dong, J., Chen, W., Wang, X., Wang, X., 2017b. Preparation of molybdenum disulfide coated Mg/Al layered double hydroxide composites for efficient removal of chromium (VI). ACS Sustain. Chem. Eng. 5 (8), 7165–7174.
Weissman, S.A., Anderson, N.G., 2015. Design of experiments (DoE) and process optimization. A review of recent publications. Org Process Res Dev. 19 (11), 1605–1633.
Xu, Z., Lu, J., Zheng, X., Chen, B., Luo, Y., Tahir, M.N., Pan, X., 2020. A critical review on the applications and potential risks of emerging MoS2 nanomaterials. J. Hazard. Mater. 399, 123057.
Yadav, V.B., Gadi, R., Kalra, S., 2019. Clay based nanocomposites for removal of heavy metals from water: a review. J. Environ. Manage. 232, 803–817.
Yadav, S., Saleem, H., Ibrar, I., Naji, O., Hawari, A.A., Alanezi, A.A., Zhou, J., 2020. Recent developments in forward osmosis membranes using carbon-based nanomaterials. Desalination 482, 114375.
Yang, Z., Qian, J., Shan, C., Li, H., Yin, Y., Pan, B., 2021. Toward selective oxidation of contaminants in aqueous systems. Environ. Sci. Technol. 55 (21), 14494–14514.
Yi, Q., Du, M., Shen, B., Ji, J., Dong, C., Xing, M., Zhang, J., 2020. Hollow Fe_3O_4/carbon with surface mesopores derived from MOFs for enhanced lithium storage performance. Sci. Bull. 65 (3), 233–242.
Yousefi, M., Gholami, M., Oskoei, V., Mohammadi, A.A., Baziar, M., Esrafili, A., 2021. Comparison of LSSVM and RSM in simulating the removal of ciprofloxacin from aqueous solutions using magnetization of functionalized multi-walled carbon nanotubes: Process optimization using GA and RSM techniques. J. Environ. Chem. Eng. 9 (4), 105677.
Yu, N., Wang, L., Li, M., Sun, X., Hou, T., Li, Y., 2015. Molybdenum disulfide as a highly efficient adsorbent for non-polar gases. Phys. Chem. Chem. 17 (17), 11700–11704.
Zangiabadi, M., Yazdapanah, N., 2021. Removal of zinc and cadmium heavy metals from industrial wastewater using organic and nano oxide adsorbents. Journal of Soil Management and Sustainable Production 10 (4), 119–136.
Zhang, X., Ding, P., Sun, Y., Wang, Y., Wu, Y., Guo, J., 2017b. Shell-core MoS2 nanosheets@ Fe3O4 sphere heterostructure with exposed active edges for efficient electrocatalytic hydrogen production. J. Alloys Compd. 715, 53–59.
Zhang, R., Liu, Y., He, M., Su, Y., Zhao, X., Elimelech, M., Jiang, Z., 2016. Antifouling membranes for sustainable water purification: strategies and mechanisms. Chem. Soc. Rev. 45 (21), 5888–5924.
Zhang, W., Shi, S., Zhu, W., Yang, C., Li, S., Liu, X., Suo, Y., 2017a. In-situ fixation of all-inorganic Mo–Fe–S clusters for the highly selective removal of lead (II). ACS Appl. Mater. Interfaces 9 (38), 32720–32726.
Zhang, T., Wang, W., Zhao, Y., Bai, H., Wen, T., Kang, S., Komarneni, S., 2021. Removal of heavy metals and dyes by clay-based adsorbents: From natural clays to 1D and 2D nano-composites. Chem. Eng. Technol. 420, 127574.
Zhao, X.-R., Xu, X., Teng, J., Zhou, N., Zhou, Z., Jiang, X.-Y., Yu, J.-G., 2019. Three-dimensional porous graphene oxide-maize amylopectin composites with controllable pore-sizes and good adsorption-desorption properties: Facile fabrication and reutilization, and the adsorption mechanism. Ecotoxicol. Environ. Saf. 176, 11–19.